NTNU
Norwegian University of
Science and Technology

Investigation of the effect of sloshing in a floating closed fish farm

Lars Gellein Halvorsen

Marine Technology
Submission date: June 2018
Supervisor: Pål Lader, IMT

Norwegian University of Science and Technology
Department of Marine Technology

Abstract

In this thesis, the effect of sloshing on the dynamic response of a floating closed containment system(FCCS) has been investigated. Results from the *SINTEF OCEANS* experiment SJØFLO have been examined and compared to numerical calculations obtained from the potential theory solver WADAM by DNVGL. In the experiment, circular cylindrical models were subject to regular wave loads, and the degrees of freedom considered were surge, heave, and pitch.

The reason for why FCCSs are being developed is that the costs related sea-lice infections in the salmon farming industry have grown tremendously over the past decade. One of the solutions to this problem is FCCS, where the farmer gets more control over the production environment. However, the FCCSs are distinctively different to the open net pen cages used in the industry today, and they pose new challenges that must be studied further to ensure that the FCCS is safe to operate and can maintain required conditions for fish well-fare.

Results show that the effect of sloshing on the dynamic response in surge and pitch is significant. However, no clear effect of sloshing was found in heave motion. The potential theory results show the same pattern, with significant effects of sloshing in surge and pitch, and no effect in heave. The results obtained in this thesis coincide with the results obtained in the end report of the SJØFLO experiment. However, as the numerical calculations have been done with different software, some deviations are present.

Finally, a spherical model was made in WADAM and analyzed for different filling levels. This analysis was done to see what effects changing filling levels of a floating structure have on the dynamic response. WADAM seemed to struggle with this type of structure, and the system was not stable until the floating collar was increased by a tenfold. Thus, care should be taken when comparing the results for the spherical model to the cylindrical one.

Sammendrag

Denne masteravhandlingen presenterer en undersøkelse av sjøegenskapene til flytende lukkede oppdrettsanlegg i bølger. Eksperimentdata fra *SINTEF OCEANS* eksperimentet SJØFLO har blitt studert og sammenliknet med nummeriske beregninger gjort i WADAM. WADAM er et program utviklet av DNVGL som baserer seg på potensial teori. Den dynamiske responsen til symmetriske modeller påvirket av regulære bølger har blitt undersøkt i jag, hiv og stamp.

Kostnadene knyttet til lakselus infeksjoner i åpne merder har økt enormt de siste årene, og nye løsninger på dette problemet er nå under utvikling. En av løsningene på dette problemet er flytende lukkede oppdrettsanlegg. Disse anleggene gir røkteren mer kontroll over produksjonsmiljøet. De flytende merdene er imidlertid forskjellig fra de åpne merdene som brukes i industrien i dag, og de bringer med seg nye utfordringer som må studeres videre for å sikre at de lukkede merdene blir trygge å betjene og at de kan opprettholde nødvendige vilkår for god fiskevelferd.

Resultater fra forsøket viser at effekten av indre bølger (sloshing) i de lukkede merdene har stor effekt på den dynamiske responsen til konstruksjonen, spesielt i jag og stamp. Det ble imidlertid ikke funnet en klar effekt av sloshing i hiv bevegelser. Resultater fra potensialteori beregninger viser det samme mønsteret, med betydelige effekter av slosing i jag og stamp, og ingen effekt i hiv. Resultatene oppnådd i denne oppgaven, sammenfaller med resultatene presentert i sluttrapporten av SJØFLO eksperimentet. Det er viktig å merke seg at de numeriske beregningene har blitt gjort med en annen programvare, og at det derfor er noen avvik.

En sfærisk modell ble ogsåundersøkt i WADAM. Denne modellen ble gitt forskjellig fyllingsgrad for å se hvordan fyllingsgrad påvirket sjøegenskapene til merden. WADAM hadde store problemer med å analysere denne typen modell, og flytekragen måtte økes med ti-gangen for at systemet skulle bli stabilt.

Preface

This thesis is written by Lars Gellein Halvorsen as the final delivery for the Master of Science degree at the Department of Marine Technology, specializing in Marine Resources and Aquaculture. The thesis has been written at the Norwegian University of Science and Technology (NTNU) in Trondheim during the spring term of 2018. The work with this thesis has been supervised by Professor Pål Lader, and the work done is meant to represent a workload of 30 ECTS.

I decided to change the topic of my master thesis after finishing the project thesis last fall. The reason for why I wanted to change topic was partly because I wanted to write a thesis that is more relevant for the aquaculture industry and partly because I wanted to learn more about hydrodynamic effects on FCCS.

I was quite new to the whole SESAM package when I started this thesis, which meant that I had to go through a long period of trying and failing before I finally got the grip of how the software worked. However, this process has in return given me a substantial learning outcome.

Trondheim, June 7, 2018

Lars Gellein Halvorsen

Acknowledgement

First of all, I would like to express my deepest gratitude to professor Pål Lader at the Department of Marine Technology for his excellent guidance during this semester. I would also like to thank SINTEF for allowing me access to the data from the SJØFLO experiment.

I would like to express my gratitude to my fellow students at the Department of Marine Technology for their unlimited assistance and support throughout all my years at NTNU. Furthermore, a special mention to Erlend Flatøy and Courtney Clark for giving me feedback on my writing during the final stage of this thesis.

A notice should also go to my girlfriend Maiken Berthelsen and my mom and dad for patiently reading through the thesis and giving me feedback.

Finally, a special message goes to my friends at office A2.023; Anders Juul Weiby and Ole Kristian Vikenes - thank you for making this a great final year

L.G.H.

Contents

Abstract i
Sammendrag ii
Preface iii
Acknowledgement iv

1 Introduction **1**
1.1 Background 2
1.1.1 Development licenses 4
1.1.2 Classification of the different Floating Closed Containment Systems 4
1.2 Objective 6
1.3 Limitations 6
1.4 Thesis outline 7
1.5 Literature review 8
1.5.1 Key design features 8
1.5.2 Methods for suppressing effects of sloshing 9

2 Theoretical background **13**
2.1 Governing equations 14
2.1.1 Hydrodynamic classification of the Floating Closed Containment System 14
2.1.2 Potential theory 16
2.1.3 Coordinate system 19
2.1.4 Equation of Motion 20
2.1.5 Transfer functions 21
2.2 Sloshing 22
2.2.1 Linear sloshing theory 22
2.2.2 Non-linear sloshing 27
2.2.3 Sloshing suppression devices 27
2.3 Dynamic response of a Floating Closed Containment System . . . 30
2.3.1 Exterior problem - Linear wave loads 31

2.3.2 Damping . . . 35
2.3.3 Internal problem - Added mass of sloshing . . . 35
2.4 WADAM . . . 36
2.4.1 Mesh Convergence test . . . 37
2.4.2 Internal Liquid Solver . . . 40

3 Experimental set-up and signal processing **41**
3.1 Test set-up . . . 41
3.1.1 Scaling . . . 45
3.2 Signal Processing . . . 45
3.2.1 Steady state period . . . 46
3.2.2 Comparison of Zero-Down cross and Spectral analysis . . . 47
3.2.3 Zero-Down cross . . . 49
3.2.4 Spectral analysis . . . 52
3.3 Rigid body motions . . . 53
3.4 Response analysis . . . 54

4 Results and discussion **57**
4.1 Sloshing modes and natural periods . . . 57
4.2 Experimental results . . . 60
4.2.1 RAO in Surge . . . 61
4.2.2 RAO in Heave . . . 62
4.2.3 RAO in Pitch . . . 64
4.2.4 Sloshing . . . 66
4.2.5 Error Sources . . . 70
4.3 Potential theory - WADAM . . . 70
4.4 The dome . . . 75

5 Conclusion **81**

6 Recommendations for further work **83**

Appendix A **II**

Appendix B **III**

Appendix C **V**

List of Figures

1.1 Global capture fisheries and aquaculture production 1991-2025, Figure created by Food and Agriculture Organization of the United Nations (2016) . . . 3

2.1 Relative importance of the different effects from wave-induced loads, Faltinsen (1998) . . . 15
2.2 Illustration of the boundaries used for the evaluation of Laplace equation. . . . 17
2.3 Six degrees of freedom with sign convention . . . 20
2.4 Cartesian coordinate system for rectangular tank . . . 23
2.5 Cylindrical coordinate system for a FCCS . . . 25
2.6 A selection of different sloshing dampers, figure created by Ibrahim (2005) . . . 28
2.7 Comparison of empirical formula and experiment for damping due to baffle ring. Figure created by Ibrahim (2005) . . . 30
2.8 Convergency test for mesh size on the circular cylinder . . . 38
2.9 Mesh convergency for the dome model . . . 39

3.1 Model . . . 43
3.2 Mooring configuration for the model experiment. Figure created by SINTEF . . . 44
3.3 Instrumentation set-up. Figure created by SINTEF . . . 44
3.4 Comparison of original- and reduced steady state period . . . 47
3.5 Methods of ocean wave analysis. Figure created by (Sundar, 2016) 48
3.6 Comparison of results from Zero-Down cross and spectral analysis 49
3.7 Figure illustrating how the ZDC and ZUC identifies each wave. Figure created by Sundar (2016) . . . 50
3.8 Zero-shifted time series with highlighted steady state period. . . . 51
3.9 Unfiltered signal plotted against the Savitzky-Golay filtered signal 51
3.10 Time series plotted in both time and frequency domain, zoomed time domain . . . 52

3.11 Spectral analysis of the response and incoming wave signal 53
3.12 Coupling effect in Surge and Pitch 54
3.13 Comparison of the different wave probes used in the reference test 55

4.1 The wave patterns associated with the six first modes of sloshing . 59
4.2 RAO in Surge calculated with experimental values for the three models K10, K11 and K21 62
4.3 RAO in Heave calculated with experimental values for the three models K10, K11 and K21 64
4.4 RAO in Pitch calculated with experimental values for the three models K10, K11 and K21 66
4.5 Sloshing RAO for the six different WP for model K11 68
4.6 Sloshing RAO for the six different WP for model K21 69
4.7 Comparison of potential theory (WADAM) and model experiment for model K10 in Surge 71
4.8 Comparison of potential theory (WADAM) and model experiment for model K11 in Surge 72
4.9 Comparison of potential theory (WADAM) and model experiment for model K10 in Heave 73
4.10 Comparison of potential theory (WADAM) and model experiment for model K11 in Heave 73
4.11 Comparison of potential theory (WADAM) and model experiment for model K10 in Pitch 74
4.12 Comparison of potential theory (WADAM) and model experiment for model K11 in Pitch 75
4.13 Comparison of wet and dry dome with 50 % filling, Surge 77
4.14 Comparison of wet and dry dome with 75 % filling, Surge 77
4.15 Comparison of wet and dry dome with 50 % filling, Heave 78
4.16 Comparison of wet and dry dome with 75 % filling, Heave 79
4.17 Comparison of wet and dry dome with 50 % filling, Pitch 80
4.18 Comparison of wet and dry dome with 75 % filling, Pitch 80

List of Tables

1.1 Table of concepts that have been approved for development licenses 5

2.1 WADAM model specifications 37

3.1 Model specifications 42
3.2 Variance calculated for the different wave probes 55

Nomenclature

Abbreviations

CFD	Computational Fluid Dynamics
DOF	Degrees of freedom
FCCS	Floating Closed Containment System
FFT	Fast Fourier Transform
GRP	Glass Fiber Reinforced Plastic
LNG	Liquid Natural Gas
RAO	Response Amplitude Operator
RAS	Recirculating aquaculture systems
WP	Wave Probe
ZDC	Zero-Down Cross
ZUC	Zero-Up Cross

Greek letters and Mathematical symbols

$\ddot{\eta}$	Translational or rotational acceleration
$\dot{\eta}$	Translational or rotational velocity
η_1	Surge motion
η_3	Heave motion
η_5	Pitch motion

γ	Maximum amplitude of the sloshing motion
$\iota_{m,i}$	Non-dimensional root of the equation $J'_m(\iota_{m,i}) = 0$
κ	Spectral parameter in the boundary condition for internal liquid
ω	Vorticity
$\omega_{m,i}$	Natural frequency of internal liquid
ϕ	Fluid velocity potential
ϕ_0	Velocity potential of internal liquid
Φ_t	Total radiation potential of a tank in WADAM
ϕ_A	Velocity potential for diffraction
ϕ_j	Velocity potential for radiation
ρ	Water Density
φ	Complex velocity potential of internal liquid
ζ	Free surface of internal liquid
ζ	Wave amplitude

Roman letters

A_b	Baffle surface area
B_{Baffle}	Damping due to annular baffle
C_D	Drag coefficient for around baffle
F_{dyn}	Hydrodynamic force
$f_{m,i}$	Free surface pattern of the natural modes of the internal liquid
F_{stat}	Hydrostatic force
J_m	Bessel function of first kind
$T_{m,i}$	Natural period of internal liquid
$\mathbf{n}$	Unit normal vector
$\mathbf{r}$	Positional vector (x,y,z)

A	Tank cross-section
g	Gravity constant
U	Current Velocity
V	Fluid velocity

Chapter 1

Introduction

The use of Floating Closed-Containment Systems (FCCS) in the production of Atlantic Salmon (*Salmo Salar* L.) has gained a considerable amount of interest over the past decade. The main reasons for the increased interest are related to the ever-growing problem with sea lice, and the increased focus on local contamination. After the Norwegian government decided to hand out production licenses to projects that could help battle either one of these issues, many new concepts were presented. Most of the new concepts that have been released are related to closed fish farming technology.

The FCCS will behave completely different in an ocean environment compared to a traditional net pen cage. Furthermore, the FCCSs are novel structures that need to be studied further to ensure safe production facilities. Thus, the seakeeping behavior of FCCSs are studied in this thesis. One should note that "Floating Closed Containment System" is a general term used to classify a broad variety of different concepts.

To give the reader some perspective on how fast this industry has grown, this chapter will start with a section presenting the most relevant background information about the aquaculture industry in Norway. The general background is followed by a section describing the most recent development of FCCS, and a presentation of the new concepts released during the first round of applications for development licenses. After that, the objectives of this thesis will be defined, together with the limitations to the scope. Finally, the thesis outline is presented at the end of this chapter with the following literature review.

1.1 Background

The Norwegian aquaculture industry started as a side project for farmers in, and around, the Norwegian fjords at the beginning of the 1960s. It took about twenty years of trial and error before the industry finally started to grow. In the period 1980 - 2015, the total Norwegian production of Atlantic Salmon went from 4 thousand tons to about 1,3 million tons.

A massive structural change to the aquaculture industry has taken place since the early beginning. Most of these structural changes came in 1991 after the Norwegian law stating: "Fish farmers cannot own the majority of the shares in more than one fish farm" was discarded (Steinset, 2017). After the law was removed, a massive consolidation took place in the following decade. Statistics show that the number of companies owning licenses for producing Atlantic salmon went from 668 in 1992 to 220 in 2005. The consolidation has continued ever since, albeit at a slower pace, and today 143 companies own at least one license. It is also important to notice the fact that the seven largest companies now hold 43% of the total licenses in Norway.

The aquaculture industry has had to solve a long list of problems to reach the production levels that are held today. The list of problem stretches from technology to diseases, to feed, to operations, etc. Even though the industry has managed to solve a lot of the issues it has faced over the years, there are still some problems that must be solved today. The most prominent obstacles are related to sea-lice, loss of fish due to escaping, local contamination and diseases. In 2016 it was reported a total cost of 5 billion NOK related to sea-lice alone, a cost that is expected to increase even further in the coming years.(The editorial team, Hegnar.no, 2016)

Norwegian aquaculture is part of a global market, and it is important to take a look at the global situation to get a better understanding of the world supply and demand for fish. The *Food and Agricultural Organization of the UN* issues a publication every other year called *"The state of the world's fisheries and aquaculture"* (Food and Agriculture Organization of the United Nations, 2016). This publication contains information about the fish production in different sectors, consumption, markets, etc., and it is highly suggested reading this publication to get a broad understanding of the status of the worldwide aquaculture industry.

Some of the key facts presented in the report by Food and Agriculture Organization of the United Nations (2016) are; aquaculture is the fastest growing animal producing industry with an increase of 37% over the past decade. In Figure 1.1

the global captures and aquaculture production from 1991 to 2025 is presented. The graph indicates that the world will see increased production of farmed fish, while the captures for human consumption will stay at the same level as of today. In the report, it is estimated that the Norwegian aquaculture will have an increase of 48% between 2013 and 2025 (Food and Agriculture Organization of the United Nations, 2016). Most of the fish stocks are fully exploited already. Thus a bigger contribution from aquaculture is needed if the consumption of global seafood is to increase.

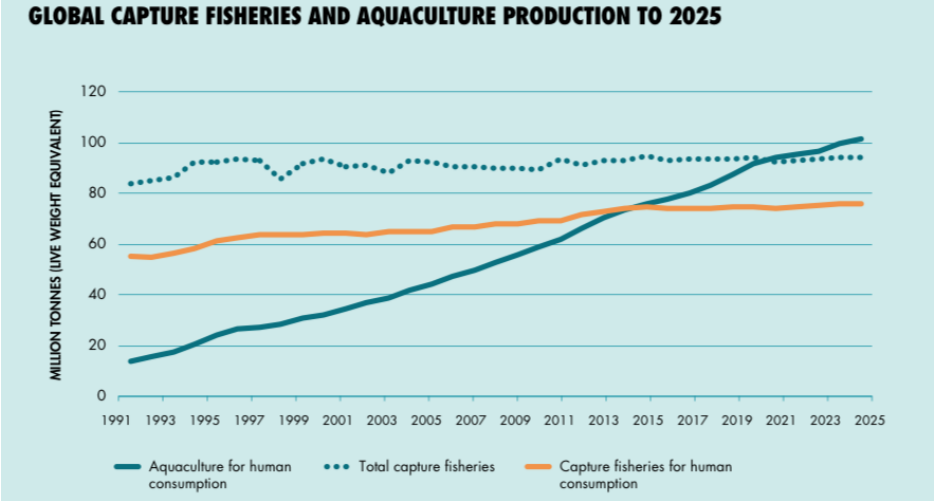

Figure 1.1: Global capture fisheries and aquaculture production 1991-2025, Figure created by Food and Agriculture Organization of the United Nations (2016)

The report by Almaas et al. (2012) predicts a six-fold increase in the added value from the aquaculture industry in Norway by 2050. The increased added value is estimated based on several different global trends, initiatives and unexploited possibilities in Norway. The unexploited possibilities are found within cultivation of different species, the supplier industry and the potential for further growth in salmon aquaculture. Some of the critical points for increased production within aquaculture are: increased world population, increased upper-middle class, an increased focus on health and the environment.

1.1.1 Development licenses

When the Norwegian government announced that they would hand out licenses to new concepts that could provide a solution for either the sea-lice or the contamination problem, the innovation rate within the industry reached new heights. 105 applications came in during the first round that ended November 2017. (Thorbjørnsen and Litland, 2017)

At the time this thesis was written (January-June 2018), 63 concepts are still to be reviewed by the Norwegian Directory of Fisheries, seven concepts have been permitted to start production, six have been given partial permission, and 29 have been dismissed. Of the 13 concepts that have either been partially or fully cleared, six are considered to be closed cages, and one is considered semi-closed. The remaining six concepts are either related to offshore fish farming or new types of open constructions. These open concepts would all be fascinating to study further from a hydrodynamical perspective. However, this thesis is focused on the closed fish cages. The open concepts will not be discussed further.

1.1.2 Classification of the different Floating Closed Containment Systems

As mentioned earlier, the term "Floating Closed Containment System" is somewhat vague, as it represents two different things depending on the field of study. From a biological perspective, FCCS says something about the interaction between the enclosed fish and the surroundings. From a hydrodynamical perspective, a FCCS says something about how water flows through the structure. According to the definitions presented by Rosten et al. (2011), a FCCS is a cage with a physical barrier that separates the production volume from the surrounding volume. The physical barrier can either be completely water-tight or partially permeable. To clarify even further, one can divide the structures into two groups based on the permeability attributes of the physical barrier and get semi-closed fish cages and closed fish cages. Returning to the hydrodynamical definition, one can say that a semi-closed structure is a structure that allows for water to escape through parts of the structure, i.e., through the bottom. A closed fish cage does not allow water to escape through the structure (other than the water exchange done by pumps). The FCCS will differ significantly from traditional net pen cages both when it comes to how the structures interact with the ocean environment, but also the daily operations of the farm will change.

It is necessary to divide the concepts that have been approved for development licenses into different groups. All closed cage concepts that have either been approved or partially approved for development licenses are listed in Table 1.1.

Table 1.1: Table of concepts that have been approved for development licenses

Concept name	Closed/semi closed	Geometry	Material
Hydra	Closed down to 20m	Cylinder	Steel
Egget	Closed	Egg shaped	Composite
Marine Donut	Closed	Cylinder/Torus	Steel
Pipefarm	Closed	Horizontal Cylinder	Steel
Stadionlaks	Closed	Half sphere	Concrete
Aquatraz	Semi-closed	Cylinder	Steel
Aquadesign	Closed	Group of cylinders	Concrete

From a hydrodynamical perspective, many factors affect how the concepts will behave in a sea environment. The most important factors are; geometrical shape, free-surface, size, and material. Free-surface is present in all of the concepts presented in Table 1.1, although some of the concepts operate with a reduced free-surface. Size is not given for all the concepts, but from the information available, it is clear that the size varies significantly. However, all of the concepts are big enough to be classified as large volume structures, which is discussed further in Chapter 2.1.1.

There are three different material types presented; steel, concrete and composite. Composite is a non-specific term that describes a variety of different attributes. However, it is likely that the composites referred to are similar to the ones used in similar structures, which is Glass Fiber Reinforced Plastic (GRP) . The material selection will influence the elasticity of the structure, which in turn might influence the dynamic response of the internal liquid.

The geometrical shape is important from several perspectives. It will define how large the free-surface is, which in turn might affect sloshing in the structure. Furthermore, it will influence how forces and stress affect the structure, and therefore also fatigue.

1.2 Objective

The intention of this thesis is to gain better knowledge of the hydrodynamic response of FCCSs in waves. The FCCSs are very interesting from a hydrodynamical perspective because they are large volume structures with a large free-surface. This type of structure is quite unique as very few other structures have such a high ratio of free surface area to structure size. However, the industry seems willing to invest heavily in FCCS farming, which makes this highly relevant. A large free-surface has proven to be a problem in other types of constructions like LNG tankers etc. Thus, the seakeeping behavior of the structure with special attention to the coupling between structure motions and liquid sloshing will be investigated in this thesis. The full list of the objectives of this thesis are:

1. Perform a literature study on the design of FCCSs and common sloshing suppression methods
2. Present the theory behind the dynamic response of a floating closed fish cage.
3. Recalculate the rigid body motions from the experiment SJØFLO conducted by SINTEF Ocean.
4. Calculate the rigid body motions with a potential theory software and compare the results to the ones obtained from the experiment.
5. Identify design elements that can improve the dynamic response of a closed fish cages.
6. Perform a parameter study on the selected concept(s) and compare to the standard circular cylinder.

1.3 Limitations

The topic of this thesis changed after the completion of the project thesis written during the fall semester as the topic of this thesis was found to be more interesting, and more relevant to the industry. However, this made it hard to find enough time to conduct an experiment of my own. It was not enough time to do a response test of the new concepts introduced in this thesis. The experiment described in this master thesis was conducted by SINTEF Ocean, and I did not have any influence on the experiment.

Several physical phenomena can be encountered related to sea loads on closed fish cages. This thesis will only focus on first order wave loads on the structure and internal waves (sloshing). Second-order wave forces, current forces, and wind forces may all be interesting to study from a hydrodynamical perspective, but as they will have a limited effect on sloshing, these loads are considered to be outside the scope of this thesis. The numerical calculations are done using WADAM, a program in the SESAM package developed by DNVGL, which has a potential theory solver.

1.4 Thesis outline

The final part of this introduction chapter contains a literature review of FCCSs. The most important design features are identified, as well as the different sloshing suppression devices used in other fields of engineering.

Chapter 2 presents the theoretical background necessary for the reader. The theory chapter is divided into four main sections, where the first will introduce the potential theory and the conditions for potential theory. The second part of this chapter describes the different effects that influence the hydrodynamic response of a FCCS. Furthermore, the third part of this chapter presents the sloshing phenomenon, together with a more in-detail description of linear sloshing. Finally, the numerical software WADAM by DNVGL is introduced together with the theory and assumptions used by the software.

The 3rd chapter describes the experiment conducted by SINTEF in-detail. In addition to the experiment description, this chapter describes the two methods used to calculate the Response Amplitude Operators (RAO). The methods used are the spectral analysis and the zero-down cross method. Furthermore, the chapter contains a brief introduction to possible error sources from the experiment.

The 4th chapter presents all results found from both the experiment and WADAM in addition to a discussion of the results individually.

Chapter 5 and 6 are the chapters that present the conclusions and the recommendations for further work on the topic respectively.

1.5 Literature review

The following section will, as mentioned above, discuss the most important design features for a FCCS, and possible sloshing suppression devices found in the literature.

All the different concepts that have been approved for development licenses, mentioned in Section 1.1.2, have a set of attributes that make up the complete design. This set of attributes make a concept more or less suited for a task, which in this case is to farm Atlantic salmon. This section will start be introducing the features that must be present in all kinds of FCCS.

1.5.1 Key design features

Closing the walls of a fish cage will give the farmer increased control over the production environment. However, the increased control implies increased complexity to the whole system (Boulet et al., 2010). Most of the key design features of a FCCS are related to control of water parameters. Based on the information presented by Rosten et al. (2011), a system for control and manipulation of the production environment is absolutely necessary for a FCCS.

The oxygen consumption is perhaps the most critical water parameter to keep track of in closed cage fish farming. According to Rosten et al. (2011) it has been shown that the consumption of oxygen depends on factors like; the size of the fish, temperature, growth rate, feed consumption, swimming velocity, and stress. Bergheim et al. (1992) has shown that internal current and swimming velocity are two of the most important factors concerning oxygen consumption and metabolism. The recommendations for oxygen levels in closed cage farming vary significantly, depending on the method used to establish the recommendations. However, there is a general agreement that too low oxygen levels could reduce growth and increase death rates, while too high oxygen levels might increase oxidative stress which in turn may lead to reduced growth and increased death rates.

The second most important factor that must be controlled is the amount of carbon dioxide that accumulates in the water. High level of CO_2 have proved to reduce the growth rate of salmon, and very high levels may lead to a higher death rate. Thus one should plan on having a system for removing carbon dioxide in a closed fish cage. According to Rosten et al. (2011) it was found that the amount of CO_2 in water increased by 1.1mg/l pr mg consumed oxygen. Thus, one can

use the oxygen consumption to estimate the CO_2 production when designing a system for removing carbon dioxide in a FCCS. Furthermore, Thorarensen and Farrell (2011) have found an acceptable maximum level of CO_2 to be 10 mg/l for post-smolt production.

Ammonia exists both as NH_3 and as NH_4^+-ions in a fish cage, thus it is common to talk about Total Ammonium Nitrogen(TAN). NH_3 is by far the most poisonous, but both NH_3 and NH_4^+ will affect the fish well-fare to such degree that it must be designed for (Chadwick et al., 2010). One solution to this issue can be a recirculation system of the water with a biofilm that transforms the NH_3 to nitrate. However, nitrate can also be poisonous for salmon if it reaches certain levels. Experience from the land-based Recirculating Aquaculture System (RAS) technology would suggest that as long as the water contains salt, the problem is reduced significantly (Rosten et al., 2011).

An issue that is partially linked to the water parameter is fish density within the cage. The requirement proposed by the Norwegian standard for net pen cages (NS9415) is $25kg/m^3$ for an open net cage (Standard Norway, 2009). However, scientists do believe that the fish can thrive with a density up to three times as high in FCCSs as long as the water parameters are kept within recommended limits (Hosfeld et al., 2009) and (Graven, 2016). It is important to notice that the experiments conducted to date have been done on parr[1] only. Thus, further research should be done before building such a high-density system. The conclusion presented in Thorarensen and Farrell (2011) with regards to fish density is that growth rate and survival will not be limiting factors for density below $80kg/m^3$, it would rather be the technical challenges and cost of maintaining acceptable water quality. Furthermore, the directory of fisheries must change the requirements for this to be a legal farm. The fish density is one of the most critical factors for the FCCSs, as both the control systems and the income depend on this factor.

Other design features that appear in all FCCS are, for instance, systems for waste removal, artificial lighting, etc.

1.5.2 Methods for suppressing effects of sloshing

As mentioned earlier, sloshing is a phenomenon that must be accounted for when designing a moving tank with a free surface, as it is cyclic load that can lead to

[1]Parr is a young salmon. The definition is used for salmon during the last stage of the freshwater period and just after smoltification is complete

structural failures etc. Thus, several methods for suppressing the effects of sloshing have been introduced in the literature. Some examples of different sloshing suppressors can be found in Figure 2.6.

As the FCCS is still a novel structure, not much research have been conducted on sloshing suppression for a FCCS specifically yet. However, by looking at other industries, like the aeronautical- and the Liquid Natural Gas (LNG) industry, one can find several methods that have been thoroughly studied.

The most used sloshing suppression devices in the aeronautical industry have been presented by Abramson (1969) together with the parameters that influence the sloshing suppression. Furthermore, both Faltinsen and Timokha (2009) and Ibrahim (2005) have described most of the sloshing devices used, and their corresponding effects on the dynamical response of the tank.

Introducing a baffle on the inside of the tank is probably the most used method for sloshing suppression in the aeronautical industry, and the different types of baffles used are presented in (Abramson, 1969). Experimental results confirming the damping effects, provided by the baffles, can be found in (Garza and Abramson, 1963). Furthermore, a semi-empirical equation for damping due to annular baffle rings was presented by Miles (Ibrahim, 2005). This equation has later been verified for low frequency sloshing by (Yang and West, 2016). The theory related to the damping due to ring baffles can be found in Section 2.2.3. However, as the damping of the baffle rings are due to viscous effects, this will not be analyzed in WADAM.

One example of a sloshing suppression method used in the LNG industry, is the anti-sloshing blanket presented in (Said et al., 2017). This method is rather difficult to implement for a FCCS, as the salmon would be restricted from reaching the free surface. However, a system where the anti-sloshing blanket is only lowered to the free surface during the worst weather conditions may work.

The sectioned tank method consists of dividing the tank into separate compartments (Abramson, 1969). Dividing the FCCS into compartments would make the control system way more complex, as the water parameters of the different compartments must be continuously evaluated. Different pumps for all the compartments must also be installed to ensure a satisfying internal current.

Reducing the free surface of the tank will alter the natural period of the structure (Faltinsen and Timokha, 2009). This method is very good from an operational point of view, as no additional internal structures could influence the fish wellfare. One way to implement the reduced free surface method is to increase the

filling level of a spherical cage above 50%. The damping of the sloshing motion, due to the reduced free surface, will be studied further and the concept is denoted "The dome" in the rest of this thesis. The model specifications can be found in Section 2.4.1, and the results from the potential theory analysis can be seen in Section 4.4

The systems mentioned above are all passive systems that are designed to take away the worst effects of sloshing. However, to be able to keep the water exchange at a sufficiently high level, an active pump system is required. One could imagine using these pumps with a control system to counteract the internal liquid in the same way as a dynamic positioning system on a vessel. A system like this is somewhat complicated, and will undoubtedly increase the power consumption of the farm significantly. Another uncertainty factor is how capable the pumps are at slowing down the water movement, and if it can respond quickly enough to combat the ever-changing perturbations.

Chapter 2

Theoretical background

Traditional net pen fish cages are slender structures with a flexible floating collar that allows for deformations when affected by sea loads (Kristiansen et al., 2015). Both the net and the flexible floating collar are designed so that they can deform when a wave hits the structure. The deformations of the structure imply that hydroelasticity is important. Hydroelasticity was first introduced by JR and Abramson (1959), as the naval counterpart to aeroelasticity, where the pressure from the fluid acting on the structure changes its state, and the change of state will again alter the pressure field around the structure. By closing the walls of the cages, the structure will become more rigid, and waves will no longer move freely through the structure. The effect of hydroelasticity will be reduced with the reduced elasticity of the structure. However, the solid walls of the structure will increase other hydrodynamic loads as radiated and diffracted wave forces, and add new effects like sloshing. All these effects will be discussed throughout this chapter.

This chapter is divided into four main sections, all of which intends to give the reader a better understanding of the seakeeping behavior of a FCCS. The first section intends to show how the FCCS can be classified from a hydrodynamic point of view. This hydrodynamic classification is the basis for most of the assumptions used in this thesis. The assumptions will be presented together with the coordinate system applied throughout this thesis. Furthermore, the potential flow theory is presented with the coinciding assumptions. Finally, in the first part, the equation of motion is defined together with transfer functions for a one degree of freedom (DOF) system.

Section two contains an overview of the sloshing problem. First, there is a general discussion about the importance of sloshing, followed by a more in-debt introduction to linear sloshing theory. The equations for finding the natural frequencies and modes with linear sloshing theory are presented together with the requirements for applying linear theory. The third part ends with an introduction to non-linear sloshing and a discussion about the validity of linear sloshing theory.

The third part of this chapter contains a brief introduction to all the hydrodynamic effects that are present in a FCCS. Both the effects of the internal liquid, and the loads from the surroundings will be defined. Not all effects are equally important; hence, a discussion of which effects can be neglected is also to be found in this section.

The last part of this section will introduce the numerical software WADAM by DNVGL and the theory behind this program. WADAM is a potential theory software specially developed for analysis of wave-structure interactions, based on the source code from WAMIT. The internal liquid solver, however, was not part of the source code from WAMIT. Thus, the theory behind this solver is presented in a separate section. The input values for both the circular cylinder and the dome models will be presented together with a discussion about the effect of the mesh size.

2.1 Governing equations

With the FCCS placed in an ocean environment, the structure will be influenced by sea loads and environmental loads. Sea loads is a general term that can be split further into current- and wave loads. The environmental loads are loads like wind etc. As stated in Section 1.3, this thesis will only focus on the first order wave loads. In the design phase, it is important to consider all loads that act on the FCCS. For further reading about the sea loads acting on a floating structure, it is advised to look at the book *Sea Loads On Ships And Offshore Structures* by (Faltinsen, 1998).

2.1.1 Hydrodynamic classification of the Floating Closed Containment System

To get a better understanding of the wave-induced loads on the FCCS, it is useful to refer to a figure like Figure 2.1. The results in this figure are based on Morisons

equation with a mass coefficient of 2, and a drag coefficient of 1 (See Equation 2.1)for a circular cylinder attached to the seafloor and penetrating the free surface (Morison et al., 1950).

$$dF = \rho \frac{\pi D^2}{4} C_M a_x dz + \frac{1}{2} \rho C_D D u|u| dz \tag{2.1}$$

The lower region in Figure 2.1, denoted wave diffraction, is calculated with diffraction theory presented in (Newman, 1962). Although the FCCSs are floating structures with a mooring system, the results in the Figure 2.1 will still give a fairly good indication as to what effects that dominate in the different wave scenarios.

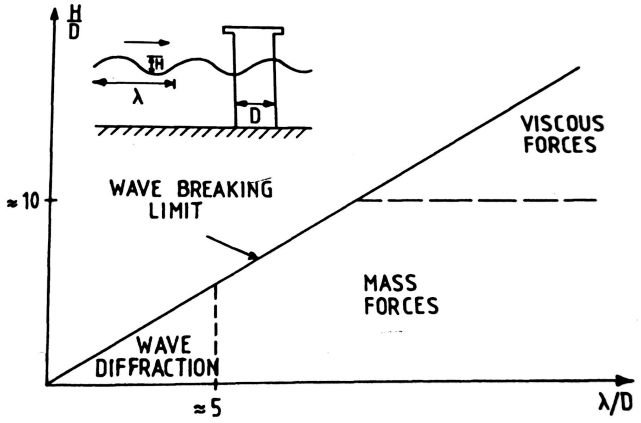

Figure 2.1: Relative importance of the different effects from wave-induced loads, Faltinsen (1998)

Lader et al. (2017) has presented an estimated significant wave height and peak period for all Norwegian aquaculture sites. 18% of all Norwegian aquaculture sites experience either large or high exposure conditions at least once a year. That is, according to the NS9415, significant wave heights between 1 and 3 meters (Standard Norway, 2009). If the FCCS is placed in conditions as presented in (Lader et al., 2017) a H/D between 1/40 and 3/40 can be expected, and the ratio λ/D is expected to lie between 30/40 and 90/40. Thus, the structure will end up in the diffraction area in Figure 2.1. The structure is in the diffraction area, which means that the diffraction forces dominate and that viscous effects are of less importance.

With the structure being far from the viscous area, as seen in Figure 2.1, it seems fair to assume that potential theory can give a satisfactory description of the dynamic response of a FCCS in the wave scenarios found along the Norwegian coastline. It is also important to notice that the figure only gives a rough classification of the relative importance of potential- and viscous flow effects. The viscous effects will be discussed further in Section 2.3, and the potential flow theory will be presented in the next section together with the assumptions necessary for applying potential flow theory.

2.1.2 Potential theory

Potential flow theory is a simplified description of the fluid flow. The three basic assumptions for potential theory are; incompressible, inviscid and irrotational fluid. To describe the fluid velocity vector at an arbitrary time, t, and at an arbitrary point, $\mathbf{x}$ = (x,y,z), one can use the velocity potential ϕ as described in Equation 2.2. $\mathbf{i}$, $\mathbf{j}$ and $\mathbf{k}$ represents the unit vectors in x, y and z respectively.

$$\begin{aligned} \mathbf{V}(x,y,z,t) &= (u,v,w) \\ \mathbf{V} = \nabla\phi &= \mathbf{i}\frac{\partial\phi}{\partial x} + \mathbf{j}\frac{\partial\phi}{\partial y} + \mathbf{k}\frac{\partial\phi}{\partial z} \end{aligned} \tag{2.2}$$

With the definition of the velocity potential, the vorticity of the fluid can be defined as presented in Equation 2.3. The fluid is irrotational if the vorticity is zero everywhere in the fluid.

$$\boldsymbol{\omega} = \nabla \times \mathbf{V} = 0 \tag{2.3}$$

If the water is to be incompressible, the continuity Equation (2.4) must be satisfied for the fluid at any given time.

$$\nabla \cdot \mathbf{V} = 0 \tag{2.4}$$

To find the velocity potential of irrotational, inviscid and incompressible fluid motion, one has to solve the Laplace equation with the correct boundary conditions. Equation 2.4 and Equation 2.2 can be combined to give the Laplace equation as presented in Equation 2.5. Furthermore, the velocity potential must

follow the Laplace equation in the entire fluid. This boundary value problem is illustrated in Figure 2.2.

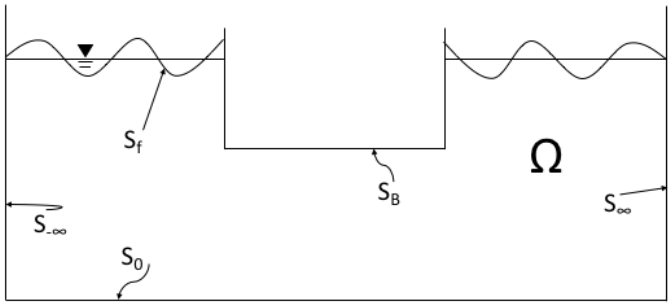

Figure 2.2: Illustration of the boundaries used for the evaluation of Laplace equation.

$$\frac{\partial^2 \phi}{\partial^2 x} + \frac{\partial^2 \phi}{\partial^2 y} + \frac{\partial^2 \phi}{\partial^2 z} = 0 \tag{2.5}$$

The pressure p in the fluid can be found by using Bernoulli's Equation 2.6. This equation is valid for any unsteady, irrotational and inviscid fluid. Positive z-axis is defined upwards, and z = 0 is defined to be the free surface.

$$p + \rho g z + \rho \frac{\partial \phi}{\partial t} + \frac{\rho}{2} \mathbf{V} \cdot \mathbf{V} = C \tag{2.6}$$

To make the calculations less complex, the time dependence from C will be included in the velocity potential. Thus, C will be an arbitrary constant function.

Boundary conditions

The boundary conditions can be seen as criteria that have to be met for the velocity potential, at the boundaries of the considered domain. The first boundary condition is known as the kinematic body condition, and it is related to the boundary between the body and the fluid domain. This boundary condition requires that no water can move through the body, or in other words, the body is impermeable to the domain fluid. The impermeability is expressed through Equation 2.7 (Faltinsen, 1998).

$$\frac{\partial \phi}{\partial n} = 0, \quad along\ the\ body\ surface(S_B) \tag{2.7}$$

The second boundary condition is the kinematic free-surface condition. This boundary condition state that any particle on the free-surface is assumed to stay on the free-surface (Faltinsen, 1998). The free-surface is defined as z = $\zeta(x, y, t)$ the kinematic free-surface condition can be expressed as in Equation 2.8. Fluid velocity has been expressed by using the velocity potential as described in Equation 2.2.

$$\frac{\partial \zeta}{\partial t} + \frac{\partial \phi}{\partial x}\frac{\partial \zeta}{\partial x} + \frac{\partial \phi}{\partial y}\frac{\partial \zeta}{\partial y} - \frac{\partial \phi}{\partial z} = 0 \qquad on \quad z = \zeta(x, y, t) \tag{2.8}$$

The third boundary condition is known as the dynamic free-surface condition. This boundary condition states that the water pressure is equal to the constant atmospheric pressure p_0 at the free surface (Faltinsen, 1998). This can be expressed by using Bernoulli's equation (as presented in Equation 2.6) with C = p_0/ρ. The dynamic free-surface condition is presented in Equation 2.9.

$$g\zeta + \frac{\partial \phi}{\partial t} + \frac{1}{2}((\frac{\partial \phi}{\partial x})^2 + (\frac{\partial \phi}{\partial y})^2 + (\frac{\partial \phi}{\partial z})^2) = 0 \qquad on \quad z = \zeta(x, y, t) \tag{2.9}$$

Looking at the boundary conditions for the free-surface, it can be observed that both 2.8 and 2.9 are non-linear equations. However, if zero forward speed and zero current in the fluid domain is assumed, the free surface conditions can be linearized. The linear free-surface conditions are presented in Equation 2.10 and Equation 2.11.

$$\frac{\partial \zeta}{\partial t} = \frac{\partial \phi}{\partial z} \qquad on \quad z = 0 \tag{2.10}$$

$$g\zeta + \frac{\partial \phi}{\partial t} = 0 \qquad on \quad z = 0 \tag{2.11}$$

The two linear free-surface conditions, Equation 2.10 and Equation 2.11, can be combined to give one free-surface condition. The velocity potential is assumed oscillating harmonically in time with a circular frequency ω. The combined free surface condition can be written as in Equation 2.12 (Faltinsen, 1998).

$$-\omega^2\phi + g\frac{\partial \phi}{\partial z} = 0 \qquad on \quad z = 0 \tag{2.12}$$

2.1.3 Coordinate system

Before describing the different loads that work on the FCCS in detail, it is essential to define both the coordinate system and the rigid body motions. A body-fixed, right-handed, coordinate system with positive Z-axis upwards through the center of gravity of the FCCS and with origin in the undisturbed free surface is used. Furthermore, the translatory motions in x-, y- and z-direction of the origin are be denoted η_1, η_2 and η_3 respectively. η_1 represents the Surge displacement, η_2 represents Sway displacement and η_3 represents Heave displacement. The angular motions about the x-, y- and z-axis are denoted η_4, η_5 and η_6 respectively so that η_4 is Roll, η_5 is Pitch and η_6 is Yaw. In figure 2.3 one can see a graphical representation of the six DOF .

With the definitions above in mind, the motion of any arbitrary point P on the body can be expressed as in Equation 2.13.

$$s = \eta_1\mathbf{i} + \eta_2\mathbf{j} + \eta_3\mathbf{k} + \boldsymbol{\omega} \times \mathbf{r} \tag{2.13}$$

Where $\times$ represents the vector product and $\boldsymbol{\omega}$ and $\mathbf{r}$ are:

$$\boldsymbol{\omega} = \eta_4\mathbf{i} + \eta_5\mathbf{j} + \eta_6\mathbf{k} \qquad \mathbf{r} = \mathrm{x}\mathbf{i} + \mathrm{y}\mathbf{j} + \mathbf{k}$$

Where **i**, **j** and **k** are unit vectors along the x-, y- and z-axis respectively. Thus, the motion of any point can be described by Equation 2.14

$$s = (\eta_1 + z\eta_5 - y\eta_6)\mathbf{i} + (\eta_2 - z\eta_4 + x\eta_6)\mathbf{j} + (\eta_3 + y\eta_4 - x\eta_5)\mathbf{k} \tag{2.14}$$

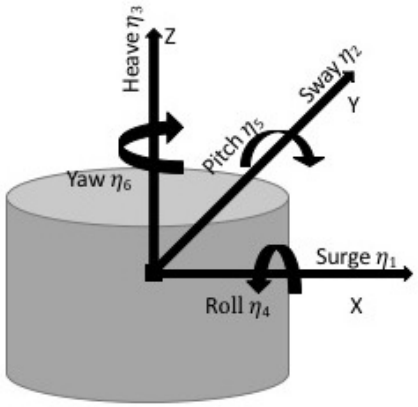

Figure 2.3: Six degrees of freedom with sign convention

2.1.4 Equation of Motion

The six degrees of motion for a FCCS are presented in Figure 2.3. The corresponding motion can be described by Newton's second law as:

$$\mathbf{M}\ddot{\boldsymbol{\eta}} = F_{stat} + F_{dyn} + F_{env} \tag{2.15}$$

with F_{env} being the environmental forces that act upon the FCCS. F_{stat} represents the hydrostatic term, F_{dyn} represents the hydrodynamic term acting on the FCCS. The hydrostatic term can be modeled as spring stiffness, and the hydrodynamic loads are composed by Froude-Kriloff-, radiation- and diffraction forces. $\mathbf{M}$ represents the mass of the FCCS, and $\ddot{\eta}$ represents the accelerations in the

DOFs presented in Figure 2.3. The motion in different directions for a FCCS can be found by solving these equations.

The motions of a floating structure can also be modeled as a spring system as presented in Equation 2.16.

$$(\mathbf{M} + \mathbf{A})\ddot{\boldsymbol{\eta}} + \mathbf{B}\dot{\boldsymbol{\eta}} + \mathbf{C}\boldsymbol{\eta} = \mathbf{F} \tag{2.16}$$

In the spring system ($\mathbf{M}$ + $\mathbf{A}$) represents the mass and the added mass of the FCCS respectively. Hence, the mass force and the added mass force can be written as; $(\mathbf{M} + \mathbf{A})\ddot{\boldsymbol{\eta}}$. $\mathbf{B}\dot{\boldsymbol{\eta}}$ represents the damping force in the system. Furthermore, $\mathbf{C}\boldsymbol{\eta}$ represents the restoring term of the system. Finally, $\mathbf{F}$ is a collective term for all the forces and moments that act upon the spring-system.

2.1.5 Transfer functions

The response of a structure in any of the six DOF can be expressed with transfer functions. Transfer functions are functions that express the ratio of response amplitude per incoming wave amplitude. These functions depend on the frequency of the oscillations and are normally denoted $|H(\omega_j)|$. The expression for the steady state response of a structure is presented in Equation 2.17

$$A_j|H(\omega_j)|sin(\omega_j t + \delta(\omega_j) + \epsilon_j) \tag{2.17}$$

Where, $\delta(\omega_j)$ represents the frequency dependent phase angle of the response, A_j is the amplitude of the incoming wave. ω_j is the circular frequency of the incoming waves.

The transfer function of a linear system can, according to Ochi (1990), be found as a solution of the differential equation of a vibratory system excited by a harmonic force or moment. Thus, by taking the Laplace transform of each of the terms presented in Equation 2.16, the transfer function for the spring system can be found as:

$$H(\omega) = \frac{X(\omega)}{F(\omega)} = \frac{1}{(M + A)\ddot{\eta} + B\dot{\eta} + C\eta} \tag{2.18}$$

2.2 Sloshing

A moving structure containing a fluid with a free-surface will almost certainly be affected by internal waves within the structure, also known as sloshing. Sloshing is a highly complex non-linear phenomenon with an infinite number of eigenfrequencies and eigenmodes. However, potential flow theory can in many cases give a sufficiently good description of the sloshing problem. Excitations with a frequency around the lowest natural frequency of the liquid motion, is the problem with the most practical interest (Faltinsen and Timokha, 2009). The linear sloshing theory is useful for predicting the liquid hydrodynamic pressure, forces, and moments as long as the free surface maintains a planar shape with a nodal diameter that remains perpendicular to the line of excitation (Ibrahim, 2005).

Sloshing has been thoroughly studied by engineers from several fields since the 1950s. The theory presented in this section is primarily based on the theory presented in the books "Sloshing" (Faltinsen and Timokha, 2009), "Dynamics of sloshing" (Ibrahim, 2005) and "The dynamic behaviour of liquids in moving containers" (Abramson, 1966).

Contained liquid in a moving tank may respond in several different ways, with the most important ones for a FCCS being; lateral sloshing, vertical sloshing and rotational sloshing. The lateral sloshing is antisymmetric modes of the motion that appear due to lateral- and pitch motions of the liquid container. The vertical sloshing are usually symmetric modes that appear due to heave oscillations of the tank, and the rotational sloshing appears due to instability in the antisymmetric modes (Abramson, 1966).

This thesis will focus on linear sloshing theory, and more specifically theory relevant for upright circular cylinders. However, the importance of non-linear effects in sloshing will also be discussed briefly.

2.2.1 Linear sloshing theory

Sloshing is such a complex problem that analytical solution exists only for a small selection of geometries, including upright circular cylinders and rectangular tanks. Due to the complexity of sloshing it is necessary to make some assumptions in order to find analytical solutions (Abramson, 1966). For the linear sloshing problem, potential theory is assumed valid, and the encapsulated liquid is water. Linear sloshing is considered valid for small surface elevations compared to characteristic tank length. Furthermore, the tank is considered to

be rigid, and the fluid to be homogenous. Finally, it is assumed that there are no liquid tank-roof interactions.

No tank-roof interactions is a fair assumption to make, as the FCCS examined in the SJØFLO experiment is an open structure. The stiffness of the structure can be determined under design; hence, this is also an ok assumption to make. Assuming potential theory is reasonable if the goal is to identify the natural periods. However, this assumption is not good enough when determining shape of the free surface at resonance as the viscous effects are neglected. Small surface elevations is a valid assumption as long as the liquid is not at its natural period.

The natural frequencies and corresponding natural modes of sloshing can be found by identifying the non-trivial solutions for the boundary value problem with zero tank excitations (Faltinsen and Timokha, 2009). The easiest way to derive the equations for natural frequencies is to start with a rectangular tank with origin in the center of the free surface, as presented in Figure 2.4.

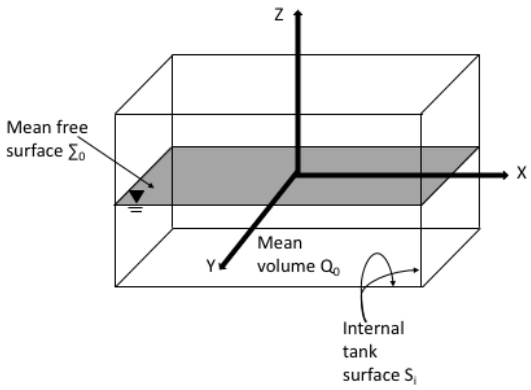

Figure 2.4: Cartesian coordinate system for rectangular tank

In Figure 2.4, Σ_0 is the mean free-surface, Q_0 is the mean liquid volume and S_i is the tank surface below the free surface. With these definitions in mind, the boundary value problem of the velocity potential is as given in Section 2.1.2. The assumption of zero tank excitation gives the requirement $\partial\phi/\partial n = 0$ on S_i with $\mathbf{n}$

being the outer normal to S_i. A second requirement is that the water inside the tank is conserved, which can be expressed as in Equation 2.19. The free-surface must follow the combined boundary condition presented in Section 2.1.2.

$$\int_{\Sigma_0} \zeta dxdy = 0, \qquad where \quad z = \zeta(x,y,t) \; determines \; the \; free-surface \tag{2.19}$$

The time-periodic solution of the linearized boundary value problem can be expressed as Equation 2.20 where ω is the circular frequency.

$$\begin{aligned} \zeta(x,y,t) &= f(x,y)e^{i\omega t} \\ \phi_0(x,y,z,t) &= \frac{ig}{\omega}\varphi(x,y,z)e^{i\omega t}, \qquad i^2 = -1 \end{aligned} \tag{2.20}$$

According to Faltinsen and Timokha (2009) it is possible to keep only the real part of the functions f and φ, without loss of generality. These solutions can be substituted into the linear sloshing problem together with the boundary conditions presented in Section 2.1.2. The result of the combination of the equations is the four equations that define the spectral boundary problem as presented in Equation 2.21.

$$\begin{aligned} \nabla^2\varphi &= 0 \quad in \quad Q_0 \\ \frac{\partial\varphi}{\partial n} &= 0 \quad on \quad S_0 \\ \frac{\partial\varphi}{\partial z} &= \kappa\varphi \quad on \quad \Sigma_0 \left(\kappa = \frac{\sigma^2}{g}\right) \\ \int_{\Sigma_0} \varphi dxdy &= 0 \end{aligned} \tag{2.21}$$

Here κ is the spectral parameter in the boundary condition. The Equation 2.21 presents a homogenous boundary problem so that there exists an infinite number of natural frequencies with corresponding natural modes.

With the spectral boundary problem defined for a rectangular tank, it is possible to look at the problem for a circular cylinder. Most FCCSs will be upright circular cylinders; hence it makes sense to work with a cylindrical coordinate

system. Cylindrical coordinate system is defined as: x = rcosθ , y = rsinθ and z = z. A graphical representation of the geometry can be seen in Figure 2.5. The spectral boundary problem presented in Equation 2.21 is presented in Equation 2.22 with cylindrical coordinates.

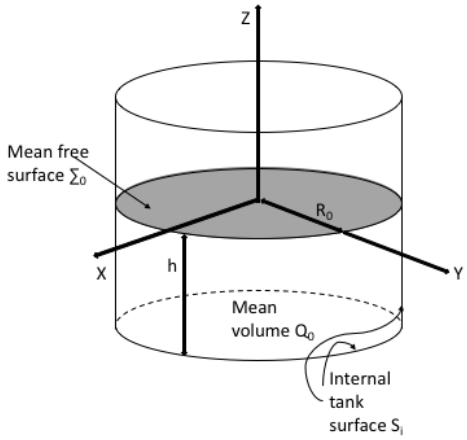

Figure 2.5: Cylindrical coordinate system for a FCCS

$$
\begin{aligned}
\frac{\partial^2\varphi}{\partial z^2} + \frac{1}{r}\frac{\partial}{\partial r}\left(r\frac{\partial\varphi}{\partial r}\right) + \frac{1}{r^2}\frac{\partial^2\varphi}{\partial\theta^2} &= 0, \quad 0 \le r < R_0, \quad -h < z < 0, \quad 0 \le \theta < 2\pi \\
\frac{\partial\varphi}{\partial r} &= 0, \quad r = R_0, \quad -h < z < 0, \quad 0 \le \theta < 2\pi \\
\frac{\partial\varphi}{\partial z} &= 0, \quad z = -h, \quad r < R_0, \quad 0 \le \theta < 2\pi \\
\frac{\partial\varphi}{\partial z} &= \kappa\varphi, \quad z = 0, \quad r < R_0, \quad 0 \le \theta < 2\pi, \\
\varphi(r,\theta,z) &= \varphi(r,\theta+2\pi,z) \\
\int_0^{R_0} r \int_0^{2\pi} \varphi(r,\theta,0)\, d\theta\, dr &= 0.
\end{aligned}
\tag{2.22}
$$

To solve the boundary value problem, separation of the spacial variables is used

so that the solution can be expressed as $\varphi = R(r)\Theta(\theta)Z(z)$.

The Laplace equation for a circular cylinder can be solved with the Bessel function of first kind, that is; R(r) = $J_m(K_r r)$ (Faltinsen and Timokha, 2009). The solution of the velocity potential is presented in Equation (2.23), and it contains the non-dimensional roots $\iota_{m,i} = k_{m,i}R_0$ of the equation $J'_m(\iota_{m,i}) = 0$. There is an infinite number of sets of these roots for every m, indexed by i counting upwards.

$$\varphi_{m,i}(r,\theta,z) = J_m\big(\iota_{m,i}\frac{r}{R_0}\big)\frac{cosh(\iota_{m,i}(z+h)/R_0)}{cosh(\iota_{m,i}h/R_0}\times\begin{cases} cos(m\theta) & ,m = 0,1,2,3..; \\ sin(m\theta) & i = 1,2,3,... \end{cases} \tag{2.23}$$

Furthermore, the free-surface pattern of the natural periods can be described with Equation 2.24

$$f_{m,i}(r,\theta) = \varphi_{m,i}(r,\theta,z) = J_m(\iota_{m,i}\frac{r}{R_0}) \times \begin{cases} cos(m\theta) & ,m = 0,1,2,3..; \\ sin(m\theta) & i = 1,2,3,... \end{cases} \tag{2.24}$$

Finally, the corresponding natural frequencies and periods can be found Equation 2.25 and Equation 2.26 respectively.

$$\omega^2_{m,i}\frac{R_0}{g} = R_0\kappa_{m,i} = \iota_{m,i}tanh(\iota_{m,i}h/R_0), \quad m = 0,1,2,..; \quad i = 1,2,.. \tag{2.25}$$

$$T_{m,i} = \frac{2\pi}{\sqrt{g\iota_{m,i}tanh(\iota_{m,i}h/R_0)/r_0}}, \quad m = 0,1,2,..; \quad i = 1,2,.. \tag{2.26}$$

2.2.2 Non-linear sloshing

Linear sloshing theory can give satisfactory results for hydrodynamic loads due to sloshing, as long as the free surface is planar. Furthermore, this theory is suited for identifying the natural frequencies and the surface elevations. However, the free surface is not always planar, and linear sloshing theory is not suited for describing the free surface effects that appear near the lowest natural sloshing frequency.

One way to investigate the non-linear effects that appear at the free surface under resonance is by applying the theory of weakly non-linear oscillations for quantitative analysis and the modern theory of non-linear dynamics for stability analysis (Ibrahim, 2005). Faltinsen and Timokha (2009) present a non-linear modal theory where the velocity potential and the free surface is expressed as linear modes and Fourier series respectively.

2.2.3 Sloshing suppression devices

As mentioned in Section 1.5.1, the large volume and the size of the free surface of the FCCS increase the possibility of having forces developed by liquid sloshing that exceeds the structural capacity. The normal frequencies of the liquid must also be controlled so that the coupling between structural components and sloshing is as low as possible (Garza and Abramson, 1963). The first mode of the liquid normal frequency can be significantly altered, and its motion can be notably dampened by sloshing suppressor devices (Garza and Abramson, 1963). There are several concepts, used in different industries today, that may be used to control the internal liquid motion. The most common types are the ring baffle system, the annular tank, floating flexible lid, a reduced free surface tank, and the sectored tank. All the different suppressors can be seen in Figure 2.6. Not all sloshing suppressors are adequate for use in a FCCS, a factor that was discussed briefly in Section 1.5.1. This section will only focus on how sloshing suppressors could work, from a hydrodynamic perspective, and more specifically on the solutions; annular ring baffle.

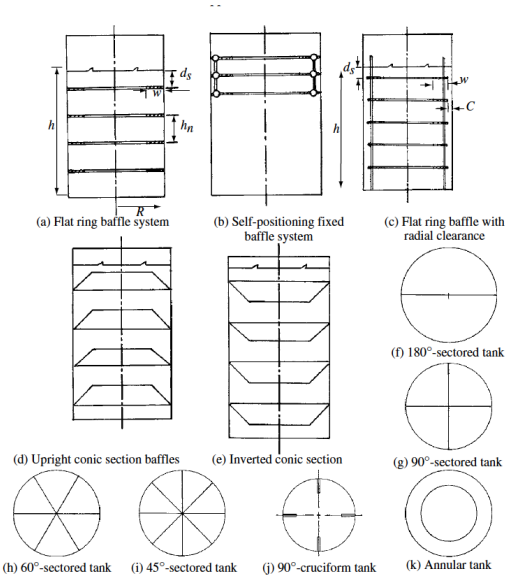

Figure 2.6: A selection of different sloshing dampers, figure created by Ibrahim (2005)

Damping of the sloshing motion due to different suppression devices is hard to determine as there are no analytical solutions that can describe the problem entirely. The damping involves the vorticity dissipation which in turn requires the full solution of the non-linear Navier-Stokes equation (Yang and West, 2016). Thus, most of the studies on sloshing suppression have been done experimentally, and lately also by the use of Computational Fluid Dynamics (CFD) software.

Ring baffle

Garza and Abramson (1963) conclude with ring baffles being a great option for any vehicle in which the first liquid resonance frequency is not critically coupled to the control system. As the FCCS is a structure without a control system as found in the space industry, this will not be a problem.

According to Ibrahim (2005), Miles presented a semi-empirical relationship for the damping ratio due to annular ring baffles in 1958. His work is based on the work conducted by Keulegan and Carpenter in the same year (Keulegan and

Carpenter, 1958). For the semi-empirical relationship to be valid, the flow around the ring baffle is assumed unaffected by the presence of the free-surface and the tank bottom. The relation is only valid for the first anti-symmetric mode, and it is expressed in Equation 2.27.

$$B_{Baffle} = C_D \phi(\lambda R, \lambda d, \lambda h) \frac{A_b}{A} \frac{\gamma}{R} \tag{2.27}$$

Here C_D is the local drag coefficient, A_b is the baffle area, R is the radius of the cylinder, and A is the area of the tank cross-section. γ is the maximum amplitude of the sloshing motion, d is the fluid height above the baffle, h is the total depth of the fluid. ϕ can be expressed as in Equation 2.28, and if h/R $>$ 1, ϕ can be approximated as in Equation 2.29

$$\phi = \frac{(4/3\pi)^3 \lambda R tanh(\lambda h)}{[1 - (1/\lambda R)^2]} \left[\frac{sinh\lambda(z+h)}{sinh\lambda h} \right]^3 \tag{2.28}$$

$$\phi \approx 0.5 e^{-5.52 d/R} \tag{2.29}$$

The drag coefficient was found to be strongly dependent on the period parameter, $\tau = U_m T/w$ (Keulegan and Carpenter, 1958). Where U_m is the time-wise maximum velocity, T is the period, and w is the width of the plate. The relation between C_D and the period parameter can be seen in Equation 2.30 and Equation 2.31

$$C_D = \frac{15}{\sqrt{U_m T/w}} \qquad for \quad 2 \leq U_m T/w \leq 20 \tag{2.30}$$

$$C_D = 2 \qquad for \quad U_m T/w > 100 \tag{2.31}$$

Finally, these expressions can be substituted into Equation 2.27, so that the damping ratio for each time scale can be obtained as in Equation 2.32.

$$\zeta = 2.83 e^{-4.5 d/R} (2 - \frac{w}{R})^{\frac{3}{2}} (\frac{w}{R})^{\frac{3}{2}} (\frac{\eta_1}{R})^{\frac{1}{2}} \tag{2.32}$$

In Figure 2.7 it is possible to observe how the semi-empirical formulation presented by Miles compares to experiment results presented by Stephens (Ibrahim, 2005).

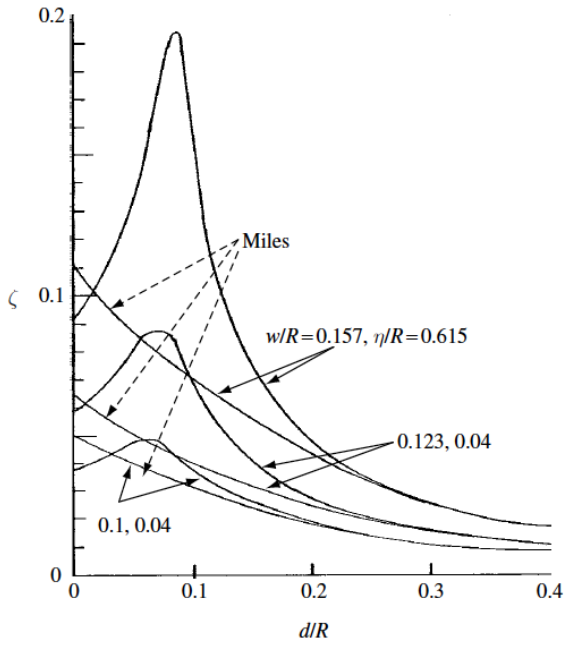

Figure 2.7: Comparison of empirical formula and experiment for damping due to baffle ring. Figure created by Ibrahim (2005)

2.3 Dynamic response of a Floating Closed Containment System

The dynamic response of a FCCS can be split into two sub-problems; the excitation loads from the surrounding water and the internal loads caused by the contained liquid. The excitation loads from the surrounding water are mainly; first-order wave forces, second order wave forces, vortex shedding from current and wind loads. Only first order wave forces will be discussed in the following section. The other loads are outside the scope of this thesis, as mentioned earlier

in Section 1.3. Three different terms of added mass can represent the internal problem, this is discussed further below.

2.3.1 Exterior problem - Linear wave loads

According to Faltinsen (1998) it is possible to obtain results from irregular sea by linearly superposing results from regular wave components. Hence it is sufficient to look at the wave-structure interaction at incident sinusoidal waves of small steepness. This problem can be split into two sub-problems;

- **Excitation**; Wave excitation loads, which can be divided further into Froude-Kriloff and diffraction forces and moments. These are the forces and moments that appears when the structure is restricted from motion in regular waves.
- **Radiation**; Added mass, damping and restoring forces and moments that appears when the structure is forced to oscillate with the same frequency as the incoming waves, without any incident waves present.

According to Newman (1962) the radiation and excitation forces can be found from the corresponding velocity potentials, which can be written as:

$$\begin{aligned} \phi(x,y,z,t) &= Re((\sum_{j=1}^{6} \eta_j \phi_j(x,y,z) + A\phi_A(x,y,z))e^{i\omega t}) \\ \phi(x,y,z,t) &= \sum_{j=1}^{6} (\eta_j \phi_j + A\phi_A) cos(\omega t) \end{aligned} \tag{2.33}$$

In Equation 2.33 ϕ_j represents the velocity potential where the body is forced to oscillate without the presence of any incident waves. The velocity potential must follow the body-surface boundary condition presented in Equation 2.7. Hence, the normal derivative of the of the velocity potential must equal the normal component of the body motion. The independence of η_j gives the following two equations according to Newman (1977).

$$\frac{\partial \phi_j}{\partial n} = i\omega n_j, \qquad j = 1,2,3 \tag{2.34}$$

$$\frac{\partial \phi_j}{\partial n} = i\omega(\mathbf{r} \times \mathbf{n})_{j-3}, \qquad j = 4, 5, 6 \tag{2.35}$$

Along the body surface S_B.

The last part of Equation 2.33 is the diffraction potential due to the incoming incident waves. The diffraction potential must follow the boundary condition of the body as presented in Equation 2.35

$$\frac{\partial \phi_A}{\partial n} = 0, \qquad on \quad S_B \tag{2.36}$$

The diffraction velocity potential (ϕ_A) can be divided further into $\phi_A = \phi_0 + \phi_D$ where ϕ_0 represents the incident wave potential, and ϕ_D represents the disturbance of the incident wave due to the fixed body. Thus, the total wave velocity potential can be written as:

$$\phi(x, y, z, t) = \phi_j(x, y, z, t) + \phi_0(x, y, z, t) + \phi_D(x, y, z, t) \tag{2.37}$$

When the velocity potentials are known, they can be used to express the oscillatory forces and moments acting on the body. To find the forces and moments, one can start by implementing Equation 2.33 in Bernoulli's equation (Equation 2.6) to find the total pressure. If only first-order terms are considered, the total pressure from Bernoulli can be written as in Equation 2.38.

$$\begin{aligned} p &= -\rho(\frac{\partial \phi}{\partial t} + gz) \\ p &= -\rho Re((\sum_{j=1}^{6} \eta_j \phi_j + A(\phi_0 + \phi_D))ie^{i\omega t}) - \rho g z \\ p &= -\rho(\sum_{j=1}^{6} (\eta_j \phi_j + A(\phi_0 + \phi_D))cos(\omega t)) - \rho g z \end{aligned} \tag{2.38}$$

After the total pressure is found, the forces and moments can be found by integrating the pressure over the wetted surface S_B.

Radiation loads

The radiation force can be written as is Equation 2.39, and for the radiation moment, $\mathbf{n}$ is replaced by $\mathbf{n} \times \mathbf{r}$

$$\mathbf{F_{rad}}(t) = -\rho Re \sum_{j=1}^{6} i\omega\eta_j e^{i\omega t} \int_S \mathbf{n}\ \phi_j dS \tag{2.39}$$

The radiation forces and moments are normally expressed in terms of added mass and damping coefficients. To find these coefficients one can combine the equation for radiation force with the boundary condition of the free surface found in Equation 2.8.

$$\begin{aligned} F_i &= Re(\sum_{j=1}^{6} \eta_j e^{i\omega t} f_{ij}) \qquad i = 1, 2, .., 6 \\ F_i &= \sum_{j=1}^{6} f_{ij}\eta_j cos(\omega t) \qquad i = 1, 2, .., 6 \end{aligned} \tag{2.40}$$

where:

$$f_{ij} = -\rho \int_{S_B} \frac{\partial \phi_i}{\partial n} \phi_j dS \tag{2.41}$$

In Equation 2.41 f_{ij} is the complex force in direction i due to the presence of the free-surface, and it depends on the frequency ω. The coefficients for added mass(a_{ij}) and damping(b_{ij}) can be written as in Equation 2.42, which in turn gives the radiation force on the form presented in Equation 2.43.

$$f_{ij} = \omega^2 a_{ij} - i\omega b_{ij} \tag{2.42}$$

$$F_i = -\sum_{j=1}^{6} (a_{ij}\dot{U_j} + b_{ij}U_j) \tag{2.43}$$

In addition to the radiation force, a hydrostatic force is found by integrating the total pressure presented in Equation 2.38. The hydrostatic force is given as in Equation 2.44, and the hydrostatic moment is found by replacing $\mathbf{n}$ with $\mathbf{n} \times \mathbf{r}$.

$$\mathbf{F} = -\rho g \int_{S_B} \mathbf{n} z dS \tag{2.44}$$

The hydrostatic force is normally expressed with restoring coefficients, in the same way as the radiation load. Thus, following Newman (1977) the total hydrostatic force and moment can be expressed as:

$$F_i = (\rho\nabla - m)g\delta_{i2} + (mz_G - \rho\nabla z_B)g\delta_{i4} - (mx_G - \rho\nabla x_B)g\delta_{i6} - \sum_{j=1}^{6} c_{ij}\eta_j \tag{2.45}$$

The δ_{ij} is the Kroenecker delta function (Newman, 1977), which is equal to 1 if j = i, and 0 otherwise. C_{ij} is a matrix with the elements presented in Equation 2.46, and the non specified elements are zero.

$$\begin{aligned} c_{22} &= \rho g S, \\ c_{44} &= \rho g S_{33} + \rho g \nabla z_B - mgz_G, \\ c_{45} &= -g(\rho\nabla x_B - mx_G), \\ c_{65} &= -g(\rho\nabla y_B - my_G), \\ c_{66} &= \rho g S_{11} + \rho g \nabla z_B - mgz_G \end{aligned} \tag{2.46}$$

For a freely floating structure, like the FCCS, c_{45} and c_{65} will disappear.

Excitation loads

The last set of forces and moments that can be found by integrating the total pressure presented in Equation 2.38 is the excitation loads. The excitation loads can be defined as:

$$F_{ex} = -\rho Re i\omega A e^{i\omega t} \int_{S_B} (\phi_0 + \phi_D)\mathbf{n} dS \tag{2.47}$$

where the moments are expressed with $\mathbf{n} \times \mathbf{r}$ instead of $\mathbf{n}$. The excitation forces are normally written as the sum of the Froude-Kriloff(ϕ_0)- and the diffraction(ϕ_D) contributions, as presented in Equation 2.48.

$$F_{ex} = -\rho(\int_{S_B} \frac{\partial \phi_0}{\partial t} \mathbf{n} dS - \int_{S_B} \frac{\partial \phi_D}{\partial t} \mathbf{n} dS) \tag{2.48}$$

2.3.2 Damping

The damping term introduced in Equation 2.16 consists of several different components. The most important component was introduced in the previous section as the damping due to wave radiation, also known as potential damping. The other damping components are related to viscous effects on the structure. For a FCCS, the friction damping and the Eddy-making damping are the two most important viscous effects (Faltinsen, 1998). Eddy-making damping appears due to flow separation that leads to vortex shedding. For a FCCS with a flat bottom, there is potential for vortex shedding at the sharp edge between the bottom and the vertical sides. However, as the motions of the FCCS are relatively slow, the damping due to vortex shedding will be relatively small.

The friction damping force is also known as the skin friction effects. This effect is most important in model scale, and can, depending on frequency and amplitude of the motion, be neglected in full-scale (Faltinsen, 1998).

2.3.3 Internal problem - Added mass of sloshing

When solving the coupled problem of sloshing and structure motion in the frequency domain, the sloshing may be expressed in terms of added mass and restoring coefficients (Faltinsen and Timokha, 2009). The added mass terms are derived in (Faltinsen and Timokha, 2009) by the use of linear modal theory. The linear modal theory transforms the boundary value problem presented earlier into a multidimensional system of ordinary differential equations.

The relation between the restoring coefficients and the added mass is presented in Equation 2.49. Hence, sloshing can be presented with either of the two coefficients. The added mass term is used further in this thesis.

$$-\omega^2 A_{kj} = C_{kj} \tag{2.49}$$

Three terms for added mass are presented, namely; the added mass of frozen liquid, added the mass of a completely filled tank and added the added mass of

the free surface. The terms for added mass can be implemented in the equation of motion for the coupled problem between the external and internal loads.

A complete set of the added mass terms can be found on page 209 and 210 in (Faltinsen and Timokha, 2009).

2.4 WADAM

Several programs have been developed for analyzing ocean-structure interactions, all of which have their advantages and disadvantages, depending on the case studied. DNVGL have developed a range of software for ocean-structure interaction called SESAM. The SESAM package is based on the finite element method and includes both time-domain- and frequency-domain solvers. *WADAM* (Wave analysis by diffraction and Morison theory) is one of the software packages developed by DNVGL, based on the source code from *WAMIT* (Wave analysis Massachusetts Institute of Technology)(DNVGL, 2015). *WADAM* is capable of analyzing floating structures of arbitrary shapes, both from a hydrostatic and hydrodynamic point of view (DNVGL, 2015). It is possible to calculate rigid body motions both with Morison theory, with 3D potential theory, and with a mix of both Morison and potential theory. The FCCS is, as mentioned earlier, a large volume structure. Thus, the 3D potential theory solver will be used in this thesis.

GeniE is another important part of the SESAM package, as it is a modeling tool made to facilitate the design of marine structures. All the modeling in this thesis has been done in GeniE before exporting to WADAM for wave analysis. Both the cylinder and the dome have been modeled as floating structures with a mooring systems corresponding to the one used in the model test. The models have been created in full-scale dimensions as presented in Table 2.1. The scaling between model and full scale has been done as described in Section 3.1.1. The water depth is selected to be 300m, implying that deep water theory is valid, i.e., no effects from the seabed.

Table 2.1: WADAM model specifications

Parameter	Dry Cylinder	Wet Cylinder	Dry Dome 50%	Wet Dome 50%
Diameter	40.5m	40.5m	37m	37m
Draught	10.125m	10.125m	18.5m	18.5m
Freeboard	4.05m	4.05m	-	-
Dry mass	1.32E+07kg	9.00E+05kg	1.4E07kg	1.25E05 kg
Vertical COG	-4.99m	-5.91m	-6.49m	-6.9m
Pitch radius	11.7m	11.5m	11.6m	14.9m
Restoring, C_{11}	131220N/m	131220N/m	131220N/m	131220N/m
Restoring, C_{55}	31886460Nm	31886460Nm	31886460Nm	31886460Nm

All the analyses have been done with fresh water conditions ($\rho = 1000kg/m^3$), to make comparisons with experiment more realistic.

The dry models were given a mass equal to the mass of the wet model(including the water), where the volume inside the cylinder was homogeneously distributed to resemble frozen water. To model the water inside the cages, a tank attribute was defined inside the walls of the structure. The tank was later filled with sea-water to a filling level equal to the water line of the structure. The tank had a free-surface, and the height from the free-surface to the roof of the tank was high enough to ensure that no water could hit the roof. In Appendix C, an illustration of the circular cylinder in GeniE, before and after meshing can be found. As one can see, the mesh looks smooth for large parts of the cylinder. However, if the mesh size is too big, it will give a poor representation of the structure, especially around the floating collar.

All analyses were done with regular waves, with periods ranging from 3s to 13s and with an interval of 0.25s.

2.4.1 Mesh Convergence test

Cylinder

A convergence test was performed for both the cylinder and the dome to find the optimal mesh size with regards to accuracy in the results and calculation time. A model with too dense mesh will require much computational power without improving the calculations. On the other side, if the mesh is too coarse, the results may be affected negatively, with appearance of singularities for instance.

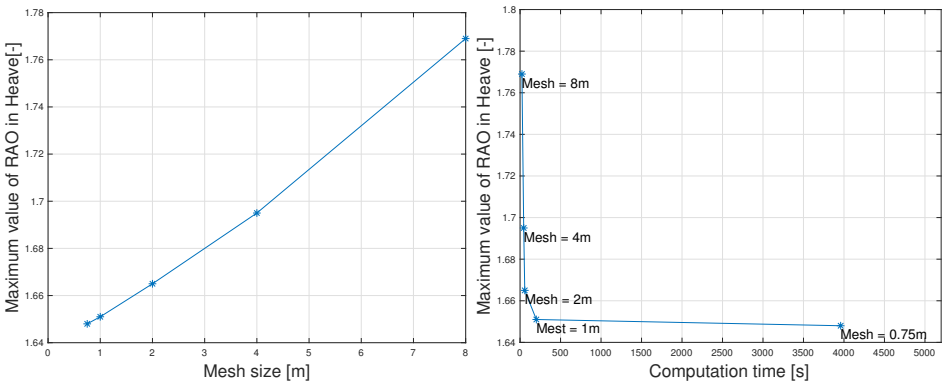

(a) Max RAO for changing mesh size (b) Accuracy vs computation time

Figure 2.8: Convergency test for mesh size on the circular cylinder

The cylinder model was tested with a mesh size ranging from 8m to 0.5m. The analysis with a mesh size of 0.5m took about 30 times longer than the one with a mesh size of 1m, and it even made the computer break down at times. Thus, the results obtained with a mesh of 0.5m are not included further. The most important results are considered to be the ones around the normal frequencies; hence the peak values are compared in the convergence test. In figure 2.8 the results of the convergence test is shown for the cylinder. A mesh size of 2 gives a maximum RAO in heave that deviates with about 1m % from the mesh size of 0.75. With the mesh size of 1m, the deviation is reduced to 0.18%. A deviation in the results of 1 % is arguably good enough. However, in this case, the number of analysis is relatively low, and the computation time with a mesh of 1m is still acceptable.

A mesh size of 1m meant that the cylindrical model was discretized by 6511 quad elements. The floating collar was modeled as a square ring with equal waterplane area and displaced volume as the floating collar used in the experiment. In Appendix C, a figure 6.2 illustrating how the complete model of the circular cylinder looks in WADAM during an analysis.

Dome

The changing filling level of the dome meant that separate geometry models had to be created for the different filling levels that were to be examined. The filling-levels analyzed in this thesis are 50% and 75%. The floating collar of the dome was also modeled as a square ring to reduce the possibility of numerical error. The initial plan was to model the floating collar equal to the one used for the cylindrical model. However, this gave a negative GM value in WADAM, which meant that the system was unstable. This factor is discussed further in the Section 4.4

The convergence test for the dome was done with a mesh size ranging from 8m to 0.5m. Figure 2.9 presents the results from the convergence test. It is interesting to see that a mesh size of 8 and 0.5 gave the same maximum value at the normal frequency. However, the curve calculated with a mesh size of 8 had some inaccuracies in the low-frequency area. Figure 2.9 shows that the curves are converging towards a maximum value of just above 1.36. Therefore, a mesh size of 1m, 0.75m or 0.5m would all give relatively good results. The mesh size used for the rest of the analysis in this thesis was 1m as this reduced the computation time from 3371s to 173s. A mesh size of 1m meant that the dome was discretized by 6631 quad elements.

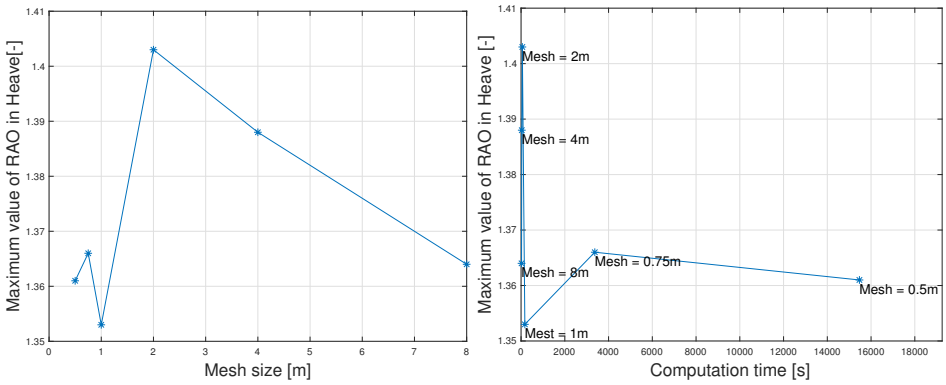

(a) Max RAO for changing mesh size

(b) Accuracy vs computation time

Figure 2.9: Mesh convergency for the dome model

2.4.2 Internal Liquid Solver

There are two ways WADAM can interpret the internal liquid in a tank, namely the quasi-static or the full dynamic method.

If the quasi-static method is selected, WADAM will calculate the harmonic pressure load on the elements inside the tank. WADAM makes use of an approximation algorithm to calculate the hydrostatic pressure distribution in the accelerated reference frame fixed with respect to the tank(DNVGL, 2015). The quasi-static method does not include effects of sloshing nor moments of inertia about the center of the fluid mass. The pressure loads are divided into an oscillating and a constant part, where the pressure gradient is given as:

$$\nabla p = \rho(\mathbf{g} - \mathbf{a}) \tag{2.50}$$

Here, $\mathbf{g}$ is the acceleration due to gravity, and if a coordinate system oscillating with the body is applied, it will have an oscillating part and a constant part. $\mathbf{a}$ is the complex acceleration of the mid-point of the tank, and ρ is the density of the internal liquid. Separating the oscillating and the constant part of the pressure gradient gives:

$$\begin{aligned} p &= \rho\mathbf{g} \quad Constant\,part \\ \nabla p_{osc} &= \rho(\mathbf{g}_{osc} - \mathbf{a}) \quad Oscillating\,part \end{aligned} \tag{2.51}$$

Since effects of the internal free surface are neglected in the quasi-static method, the full dynamic method was used in this thesis. With the full dynamic method, the restoring stiffness and the added mass of the tank are added to the global equation of motion and the global radiation potential. Thus, the pressure gradient can be written as:

$$\nabla p = -\rho(\Phi_t + gz) \tag{2.52}$$

Where Φ_t is the total radiation potential of the tank liquid.

Chapter 3

Experimental set-up and signal processing

In 2017 SINTEF Ocean conducted an experiment in the large towing tank at Tyholt named "SJØFLO" (Seakeeping behavior and mooring systems for closed fish cages abbreviated in Norwegian). The primary goal of this experiment was to study the seakeeping behavior of closed floating fish cages. Furthermore, the effects of sloshing on the rigid body motion, and the effects of flexibility in the structure were also of interest. In the experiment, five different models were used, all with the geometry of an upright cylinder as seen in Figure 3.1. The end report from this experiment is published in Norwegian (Kristiansen et al., 2018a). Also, a paper about the seakeeping behavior of a rigid floating closed fish cage has been submitted to OMAE2018 (Kristiansen et al., 2018b). This chapter will present the relevant information from the experiment set-up, the models, etc. together with the two methods used to analyze the seakeeping behavior from the experiment.

3.1 Test set-up

In the main experiment in SJØFLO, five different models were tested, of which three will be evaluated in this thesis. The experiment was conducted in the large wave tank at the center for Marine technology in Trondheim. The wave tank

measures 10.5m wide, 10m deep and 85m long, and it is fitted with a double flap wave maker at one end and a parabolic beach on the other end.

Model description

All models had the same geometrical shape, of an upright cylinder, at the scale 1:27. The first model can be viewed as a reference model, denoted K10, as it was filled with weights instead of water. Weights are supposed to represent frozen water. The second model was a stiff model, denoted K11, meant to represent a concrete structure. The last model was an elastic model, denoted K21, and it was meant to represent a GRP structure. The K11 model turned out to be a bit more flexible than first anticipated, making it more like a steel structure. This is a factor that will be discussed further in Chapter 4.

The specifications for the different models can be found in table 3.1. As the experiment is meant to be a general study of the seakeeping behavior of a closed fish farms, the full-scale size does not represent one real-world example but can be seen as a generic size.

Table 3.1: Model specifications

Parameter	Symbol	K10	K11	K21
Diameter	D	1,50m	1,50m	1,50
Draught	d	0,375m	0,375m	0,375m
Freeboard	f	0,15m	0,15m	0,15m
Mass	M	666,3 kg	48,5 kg	36,1 kg
Vertical Centre of Gravity	VCG	-0,186 m	-0,223 m	-0,277 m
Pitch Gyration radius	r_{55}	0.453m	0.495	0.495

In Figure 3.1 one can see how the coordinate system is placed on the models as described in Section 2.1.3.

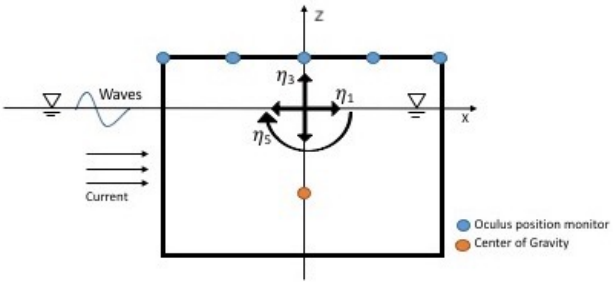

Figure 3.1: Model

Test conditions

The test conditions were the same for all three models: regular waves with wave periods ranging from 0.69s to 2.50s. The wavelengths were in the range 0.74m to 9.64m, and the tests were conducted with three different wave steepnesses; 1/30, 1/45 and 1/60. A full table of the test conditions can be found in Appendix A.

Instrumentation

All models were fastened with four mooring lines, two along the direction of the tank, and two orthogonal to the tank direction. All mooring lines were attached using a crowfoot set-up so that each model was fastened in 8 points. The set-up can be seen in Figure 3.2.

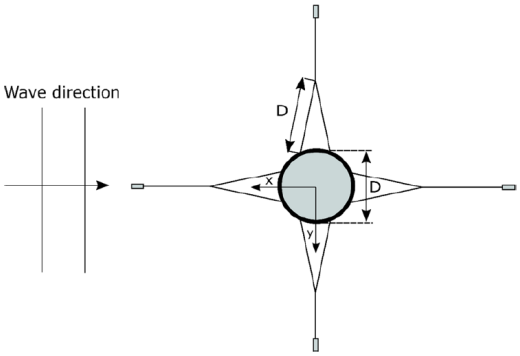

Figure 3.2: Mooring configuration for the model experiment. Figure created by SINTEF

Figure 3.3 indicates the position of all the instruments used during the tests. WP is short for Wave probe, Pos is position measurements, and acc is the accelerometers. As seen in the figure, nine positional markers gave out x, y and z positions. The three accelerometers provided x, y and z accelerations. Wave probe 1-5 gave wave height on the outside of the cage, while wave probe 7-12 gave internal wave height. The last three wave probes (13-15) were placed a distance from the model, one in front, one behind, and one towards the tank-wall.

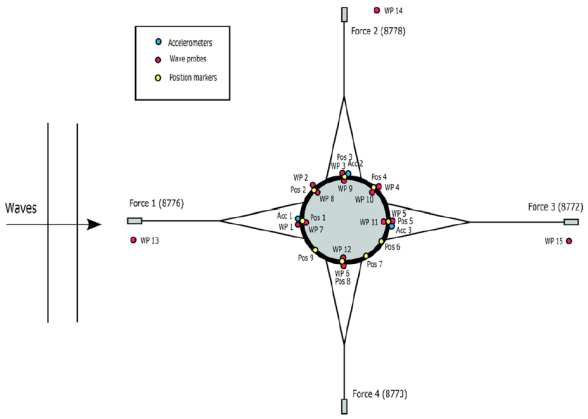

Figure 3.3: Instrumentation set-up. Figure created by SINTEF

3.1.1 Scaling

Converting between model- and full scale in the field of hydrodynamic is not a straightforward task, as the importance of different effects might be different in the two scales. However, the two most used methods for scaling hydrodynamic effects are Froude- and Reynolds scaling. The requirements for similarity, posed by the two scaling methods, can normally not be satisfied at the same time. Thus, it is important to find the dominant effect, and ensure that this effect is scaled correctly. The Froude number expresses the ratio between inertial- and gravity forces, while the Reynolds number expresses the relationship between inertial forces and friction (Steen, 2014). It is also important to make sure that the geometrical shape is maintained in the two scales.

For a net pen cage, for instance, the viscous effects are dominant. Hence, the scaling must be done with similarity in Reynolds number. However, as the FCCS have low viscous effects, and that the waves on the free-surface are gravity driven, a similarity in Froude number must be ensured in this case.

$$\frac{F_i}{F_g} \propto \frac{\rho U^2 L^2}{\rho g L^3} = \frac{U}{\sqrt{gL}} \tag{3.1}$$

The Froude number is defined as in Equation 3.1. U is the current velocity, L is the characteristic length. Knowing this definition, the dynamic similarity requirement follows the one presented in Equation 3.2.

$$\begin{aligned} \frac{U_M^2}{gL_M} &= \frac{U_F^2}{gL_F} \\ \frac{U_M}{\sqrt{gL_m}} &= \frac{U_F}{\sqrt{gL_F}} = F_n \end{aligned} \tag{3.2}$$

3.2 Signal Processing

The measurements from the experiment were collected in time-series with a sampling rate of 38.49 Hz. A steady-state period of the time-series was extracted for each test for the analysis, the selection of steady-state period will be discussed further in the next section. The wave response was calculated both in the time domain and in the frequency domain with two different methods; Zero-Down

cross(ZDC) and spectral analysis(SA). Both methods and a comparison between the two can be found in Section 3.2.2.

3.2.1 Steady state period

Steady state is defined as the period where there are no transition effects. In this thesis, the start and end of the steady state period have been calculated individually for each of the 23 wave scenarios. It is assumed that the steady state period is equal for the three wave steepnesses. The complete table of the steady state periods used for the calculations in this thesis can be found in Appendix B.

The beginning of the steady state period has been calculated following Equation 3.3 by assuming potential theory. C_p is the wave velocity, Ramp time is the time used to reach full power for the wave maker. The first four oscillations are removed as they those tend to be noisier than the rest of the signal. The distance is the distance between the wave-maker and the model. The output of this equation is a coefficient that can be multiplied with the time series to find the start point in that particular series.

$$start = \frac{(\frac{Distance}{C_p} + Ramp\,time + 4T)}{Length\,of\,time\,series} \tag{3.3}$$

Equation 3.4 is the equation used to calculate the end of the steady state period. If the value is higher than 1, the end of the steady state period is set to 1 (End of measurements). The reason for why the steady state period must be cut off before the end of the time series is because the waves will return to the model after hitting the beach and then affect the response amplitudes.

$$end = \frac{(\frac{Distance_{Wavemaker-model} + 2Distance_{Model-Beach}}{C_p})}{Length\,of\,time\,series} \tag{3.4}$$

As the steady-state period is calculated based on a theoretical approach, it is important to confirm that the measurements are at steady-state in the selected period when post-processing the data. One way to confirm the validity of the steady state period is to calculate a reduced steady-state period and compare. In Figure 3.4 the steady state period is plotted against calculations done with half of the original steady state. As seen in the figure, the deviations are relatively

small. Hence, the original steady state period seems to be valid. All steady-state periods were also plotted and confirm by eye measurements.

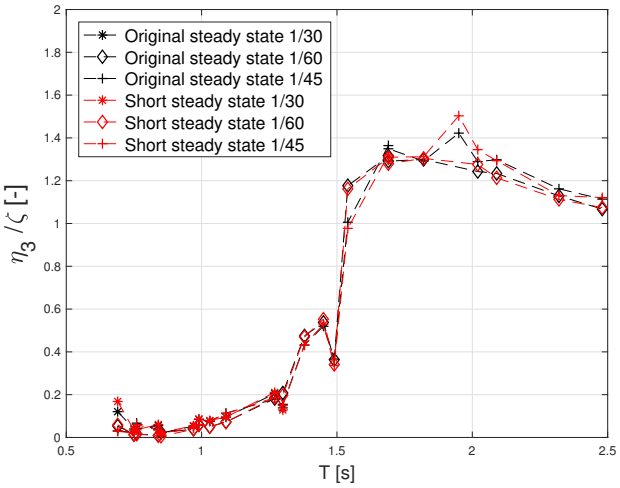

Figure 3.4: Comparison of original- and reduced steady state period

3.2.2 Comparison of Zero-Down cross and Spectral analysis

The two different methods used to analyze the wave response in this thesis are, as mentioned, the Zero-Down cross and the spectral analysis. (Sundar, 2016) has divided the different methods for wave analysis into two main branches as seen in Figure 3.5. The statistical procedures can be further divided into two different methods; the Zero-Up cross and the Zero-Down cross . It has been proven that the differences in wave heights calculated using the two methods are small. However, wave periods calculated using the two methods vary slightly more. Both the ZUC and the ZDC identify every single wave and evaluate the mean of all the single waves recorded. The statistical procedures make use of the time domain for the calculations.

The statistical methods consist of Fast Fourier Transform method and the Covariance method. The FFT method is often referred to as spectral analysis, and it is the most common of the two statistical methods. The spectral analysis makes

use of the frequency domain to identify the responses.

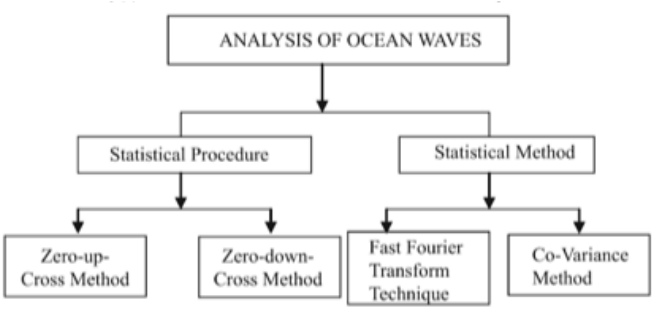

Figure 3.5: Methods of ocean wave analysis. Figure created by (Sundar, 2016)

When an experiment is conducted with irregular waves, one depends on the spectral analysis to calculate the RAOs for the different periods. However, in this case, all tests were performed using regular waves, which made it possible to use both the spectral analysis and one of the statistical procedures. In Figure 3.6 the results of the two methods are plotted against each other. It is clear to see that the two methods give more or less the same results.

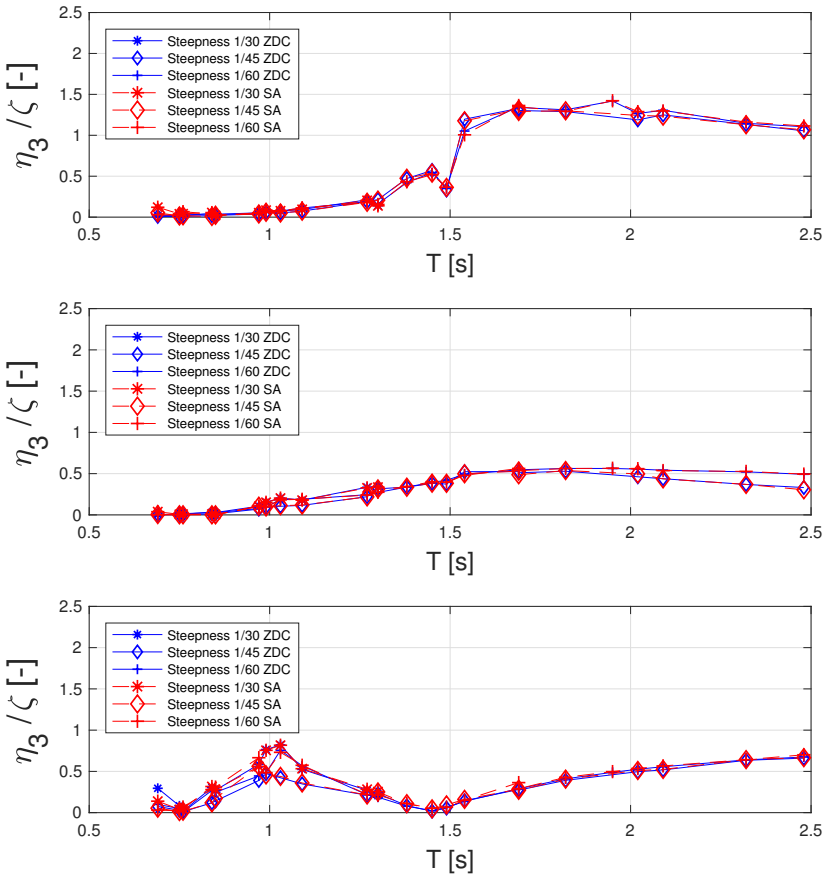

Figure 3.6: Comparison of results from Zero-Down cross and spectral analysis

3.2.3 Zero-Down cross

Figure 3.7 shows how each wave is identified with both the Zero-Up cross and the Zero-Down cross method. All the post-processing was done in Matlab, as Matlab is very well suited for signal processing.

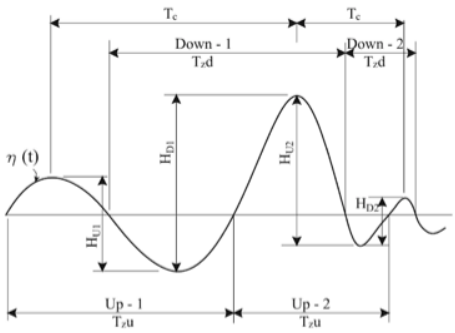

Figure 3.7: Figure illustrating how the ZDC and ZUC identifies each wave. Figure created by Sundar (2016)

As the raw-data oscillated around a number different from zero, the first step was to shift the oscillations so that the mean became zero. At the same time, the steady-state period of the measurements had to be extracted. These steps were repeated for every sensor. The selection of the beginning and end of the steady state period for each wave scenario is described in Section 3.2.1. The last step of the preprocessing of the raw data was to pass it through a filter to get rid of any measurements that were clearly wrong. The high-frequency tests had significant noise and were therefore passed through a built-in Savitzky-Golay[1] filter with varying parameters. This filter gave a smoother curve with similar amplitudes corresponding to the main oscillation of the noisy signal. Figure 3.9 shows the signal before and after filtering. As seen in the figure, the filter is not perfect, but it gives a good improvement and is considered to be good enough for the purpose of this thesis.

[1]For more information about how the filter works see:
https://se.mathworks.com/help/signal/ref/sgolay.html

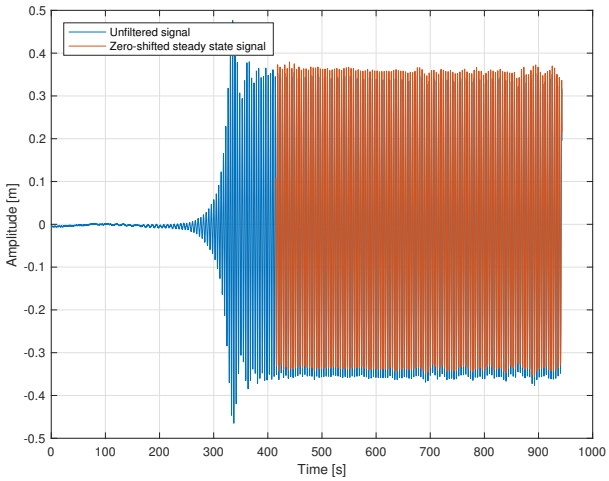

Figure 3.8: Zero-shifted time series with highlighted steady state period.

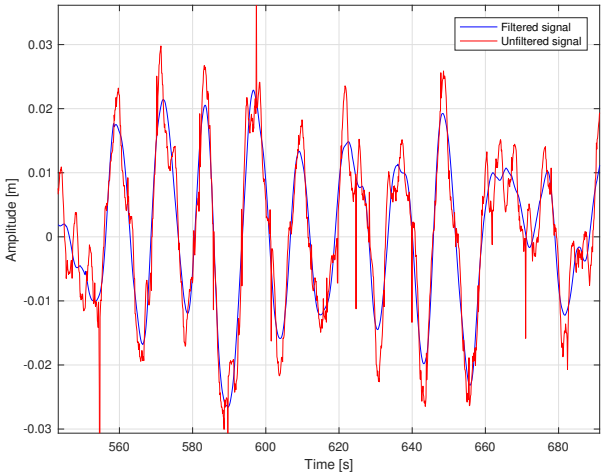

Figure 3.9: Unfiltered signal plotted against the Savitzky-Golay filtered signal

To find the amplitudes of the individual waves, all points in the measurements

where the value went from positive to negative were identified. After that, maximum and minimum values between each zero-cross were identified by the built-in max and min functions in Matlab. Amplitudes in z- and x-direction were found for the different position measurements, and for the different wave probes.

3.2.4 Spectral analysis

The spectral analysis makes use of the built-in Fast Fourier Transform function in Matlab. The function takes a time-domain signal and turns it into a frequency-domain signal as seen in Figure 3.10.

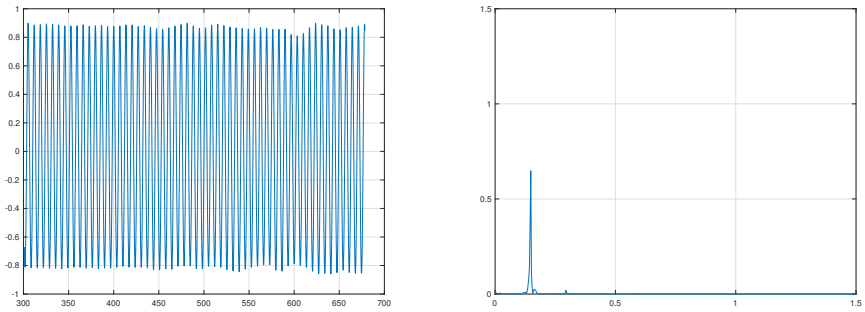

(a) Time series of incident wave

(b) FFT of the incident wave signal

Figure 3.10: Time series plotted in both time and frequency domain, zoomed time domain

Smoothing out the ends of the steady state period helps sharpen the spectral window. In this thesis, the smoothing was done by implementing a Bingham ramp function in the analysis before the Fourier transform, as described in (Newland, 1981). The Bingham ramp function weights the middle part more than the edges, which in turn smooths out the discontinuities that exist at each end.

In the Figure 3.11 the response signal is plotted against the undisturbed wave signal. The integration boundaries used to calculate the RAOs, are sat as described in Section 3.4. The figure does also show a much smaller peak at two times the normal frequency, and an even smaller peak at three times the normal frequency for the response signal. These smaller peaks are higher order normal

frequencies.

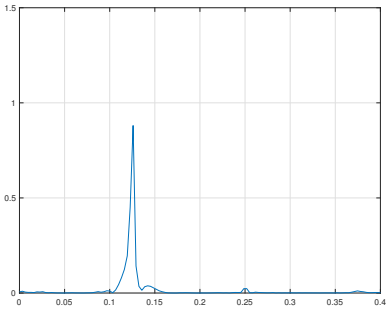

(a) FFT of the incident wave signal

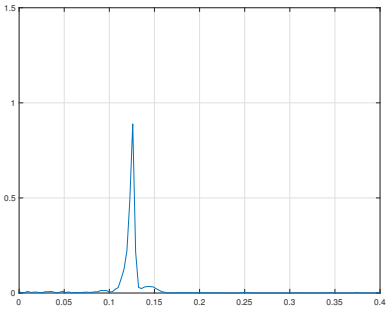

(b) FFT of the structure response signal

Figure 3.11: Spectral analysis of the response and incoming wave signal

3.3 Rigid body motions

In the experiment, the models were moored so that they were allowed to move in all 6 degrees of freedom. However, as the models are symmetrical and the waves are sent along the x-axis, the motions in the y-direction (perpendicular to the tank length) were of little interest. Thus, the motions studied from the experiments are in Surge (translation in x), Heave (translation in z) and Pitch (rotation about y), as mentioned earlier.

The heave amplitude was calculated from the average amplitude of Pos3 and Pos8 in Z-direction as in Equation 3.5

$$\eta_3 = \frac{(Pos3_z + Pos8_z)}{2} \tag{3.5}$$

The pitch amplitude was calculated by the use of Equation 3.6, where l_x is the horizontal distance between the two Oculus position monitors, and Z_{01} and Z_{05} are position in Z direction for Pos1 and Pos5 respectively.

$$\eta_5 = \frac{Z_{01} - Z_{05}}{l_x} \tag{3.6}$$

The Oculus position monitors are all placed along the upper edge of the models, which automatically shifts the coordinate systems a distance h from the free surface. It is essential to keep in mind that a shift like this will give a coupled effect in Surge. Equation 3.7 shows how the coupling effect can be corrected for. The coupling effect is also illustrated in Figure 3.12.

$$Surge = \Delta x - hsin(\theta) \tag{3.7}$$

Where Δx is the amplitude measured in the x-direction from the Oculus sensor, h is the sensor height above the free surface, and θ is the pitch angle.

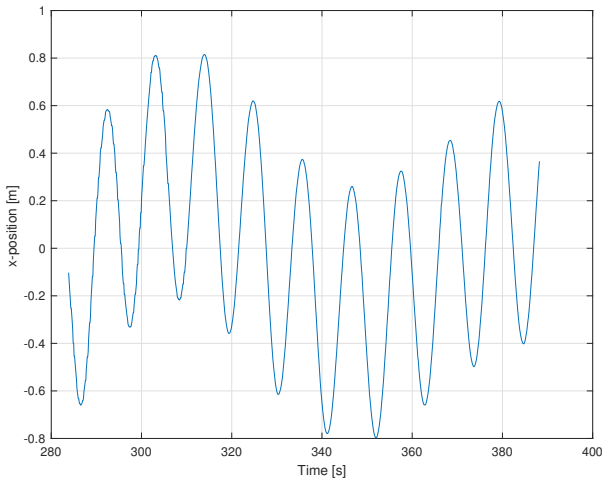

Figure 3.12: Coupling effect in Surge and Pitch

3.4 Response analysis

For the Response Amplitude Operator (RAO) calculations, the undisturbed wave amplitude ζ_a was required. A calibration run was conducted for each wave period

without a model in the tank. In the Figure 3.13 one can see measured amplitudes for the three Wave probes(13-15), and how they compare to the reference wave amplitudes. As seen in Figure 3.13 both WP13 and WP15 seem to fit the reference quite well. The least squares method was used to determine what line was the best fit for the reference line. The equation used to calculate the variance is shown in Equation 3.8.

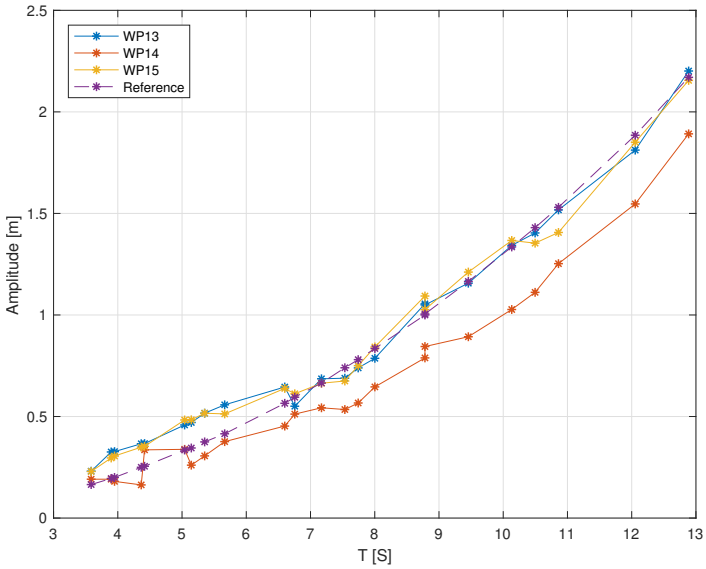

Figure 3.13: Comparison of the different wave probes used in the reference test

$$\sigma_y^2 = \frac{1}{N}\sum_{n=1}^{N}(y_n - \bar{y})^2 \tag{3.8}$$

Table 3.2 shows that WP13 is the one that fits the reference line the best. Hence, all following calculations will be done with WP13 as the source for undisturbed wave amplitude ζ_a.

Table 3.2: Variance calculated for the different wave probes

Wave probe	WP13	WP14	WP15
Variance m^2	0.0099	0.0280	0.0123

With the motions recorded in time series both for the body and the free-surface elevation, it was possible to calculate the transfer functions. Surge, Heave, and Sloshing were evaluated for the undisturbed wave amplitude, while Pitch was made dimensionless by multiplying with the dispersion relation k in the denominator. Equation 3.9 to 3.12 are the ones used to calculate the transfer functions.

$$H_1(\omega) = \frac{\eta_1}{\zeta_a} \tag{3.9}$$

$$H_3(\omega) = \frac{\eta_3}{\zeta_a} \tag{3.10}$$

$$H_5(\omega) = \frac{\eta_5}{k\zeta_a} \tag{3.11}$$

$$H_{sloshing}(\omega) = \frac{\zeta sloshing}{\zeta_a} \tag{3.12}$$

All the results from the RAO calculations will be presented in Chapter 4 together with a discussion of the different error sources present in the experiment.

Chapter 4

Results and discussion

All results obtained throughout this thesis will be presented in this chapter followed by a discussion of the different results. First, the natural periods and the corresponding modes of sloshing in a circular cylinder will be presented. The modal shapes have been calculated with linear sloshing theory (Section 2.2.1), assuming potential theory. After that, the rigid body motions calculated from the SJØFLO experiment will be presented for each of the three models. The experimental results from SJØFLO are followed by a section presenting RAOs calculated in WADAM. Finally, the results from the dome concepts introduced in Section 1.5.2 will be presented.

All results presented in this chapter will be presented in model scale unless specified otherwise. All amplitudes are given in meters, and all free surface elevations are presented in a body-fixed coordinate system as described in Chapter 2.1.3.

4.1 Sloshing modes and natural periods

In Section 2.2.1 a method for calculating the natural modes of sloshing, and the corresponding natural periods with linear theory were presented for an upright circular cylinder. Following the Equation 2.24, the wave pattern can be calculated for every mode. In the free surface calculations m = 0,1,2,.. is the azimuth mode number, and i = 1,2,.. is the radial mode number. The most interesting modes of sloshing are the ones that correspond to a natural frequency within the

frequency range of the incoming waves. Furthermore, the modes with the highest natural period are the ones that affect the dynamic response the most. When the frequency gets too high, the second-order- and viscous effects will suppress the motions. For these reasons only the wave pattern of the six modes of sloshing with the highest period have been plotted below.

The calculated natural modes and natural periods are the same as the ones presented in (Kristiansen et al., 2018a). The natural modal shapes calculated based on linear theory are expected to be equal as they are both calculated based on the same formulas presented in (Faltinsen and Timokha, 2009).

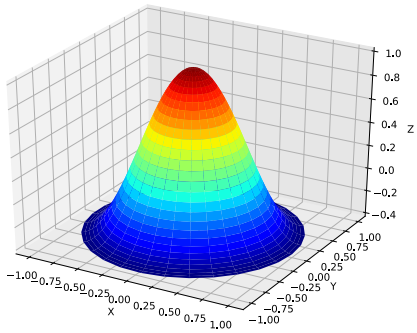

(a) $T_{0,1} = 0.907$s

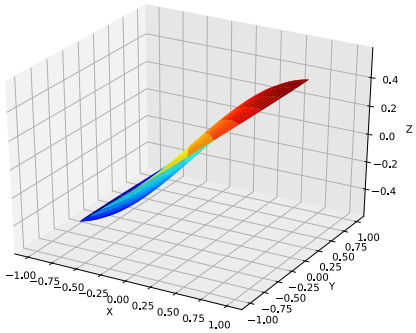

(b) $T_{1,1} = 1.502$s

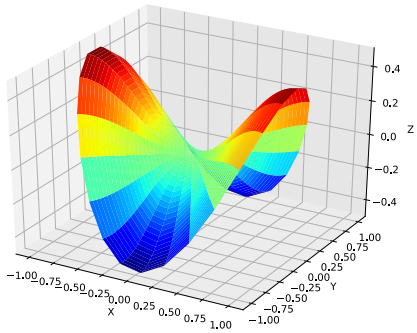

(c) $T_{2,1} = 1.042$s

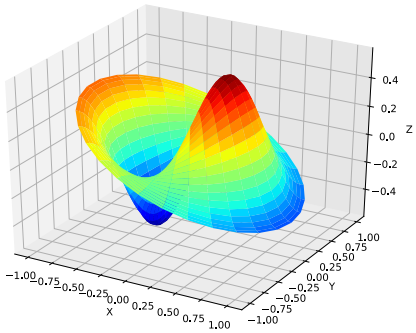

(d) $T_{1,2} = 0.756$s

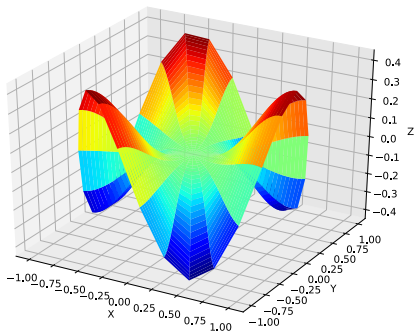

(e) $T_{3,1} = 0.860$s

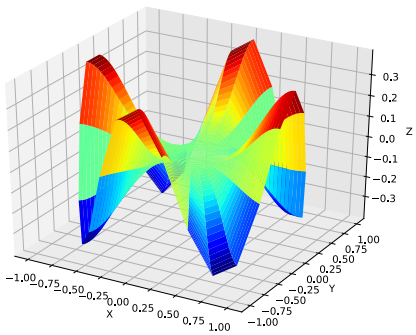

(f) $T_{4,1} = 0.757$s

Figure 4.1: The wave patterns associated with the six first modes of sloshing

4.2 Experimental results

As mentioned in Section 3.3, the models examined from the SJØFLO experiment were all symmetrical, and the waves were angled at 0 degrees with respect to the coordinate system presented in Section 2.1.3. Thus, only the motions in Surge, Heave and Pitch were of interest. The RAOs in the three DOF are calculated from the post-processed data with the spectral analysis method as presented in Section 3.2.4, and the formulas presented in Equation 3.9 to Equation 3.12. The method used to calculate the RAOs in this thesis is the same as the one used in (Kristiansen et al., 2018a). However, the filters applied to the raw data are slightly different, hence the results may deviate slightly. Most of the deviations can be seen in the area of high-frequency motions.

The results are divided into four subsections, one for each of the three DOF examined, and one for the calculations of the sloshing RAO.

Some remarks from the experiment worth noting are; the measured incident waves deviate slightly from the expected values, and the estimated steady state period was confirmed to be steady state by comparing with a shortened steady state window. The incident waves generated by the wavemaker proved to give some deviations between expected wave height and measured wave height at the model position, especially in the high-frequency area. These deviations are presented in Figure 3.13, along with the deviations in measurements by the different WPs.

For each test condition, a time window was identified as the steady state window. In the steady state window, all transient effects were expected to have died out. The selection of the steady state period is presented in Section 3.2.1. In addition to the steady state period used for the RAO calculations, a shorter steady state period was tested to see if the selection of the steady state period influenced the results. The results from the steady state comparison are presented in Figure 3.4. Looking at Figure 3.4 it is fair to say that the calculated RAOs are more or less equal for the two steady-state periods.

A plot of the calculated RAOs is presented for each of the three models in the three DOF examined. A fourth plot containing the RAOs of all three models is also presented in the three DOF. The fourth plot is presented to make it easier to compare the different model results, with regards to sloshing effects and effects of the elasticity of the structure.

4.2.1 RAO in Surge

The effect of the internal liquid(present in K11 and K21) on the RAO in surge motion is obvious when looking at Figure 4.2. A cancellation effect appears for both wet models at the natural period of the dry model giving a RAO just above zero. It should be noted that the cancellation effect appears at a lower period for the elastic model than for the rigid model, at T=1.3S and T=1.45s respectively. The natural periods of the wet models are found at approximately 1s, which corresponds well with the natural period of sloshing mode 2,1.

The RAO at the natural period for model K11 is almost 25% higher than model K21, which can be clearly seen in Figure 4.2d. The reason for this is unclear, but might be because of interaction with the elasticity in the structure for model K21. For model K11, the high-frequency sloshing mode appear at T=0.7s, which can be clearly seen for the wave steepness of 1/30 (see Figure 4.2b).

It is also interesting to observe that the RAOs calculated at periods higher than 2 seconds are equal for the three models.

Comparing the calculated RAO in surge to the results presented in (Kristiansen et al., 2018a), the results are more or less the same with only minor deviations at the lower periods. As mentioned earlier, the small deviations are most likely due to the different filters that have been applied.

The sudden drop in response for model K10, with a wave steepness of 1/30, between 1.2s and 1.4s is most likely due to an error in the measurements.

Finally, the steepness seems to influence the RAOs significantly, especially for the two wet models. For model K21, a steepness of 1/60 gives less than half of the RAO for a steepness of 1/30. A steepness of 1/45 lies between the two others. The same pattern can be seen for K11; however, the steepness of 1/45 has a peak that reaches almost as high as the highest peak of 1/30. Model K10 seems to be unaffected by this factor, which can be seen in Figure 4.2a .

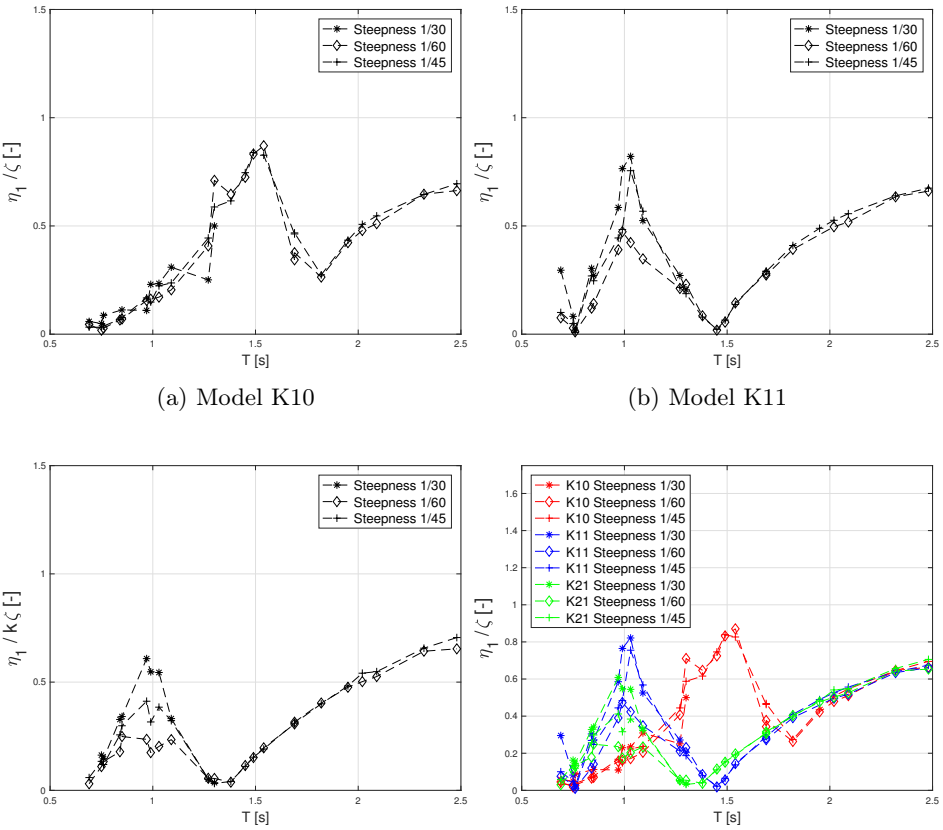

(a) Model K10

(b) Model K11

(c) Model K21

(d) Comparison of the three models

Figure 4.2: RAO in Surge calculated with experimental values for the three models K10, K11 and K21

4.2.2 RAO in Heave

The RAOs in heave calculated with the experimental results are presented in Figure 4.3. Looking at the comparison of the three models, all RAOs have the same shape and a natural period of around 1.8s. Thus, there is no effect of sloshing on the heave RAO. The fact that sloshing did not affect the RAOs in heave was expected as the internal liquid translates in phase with the structure. This is well in accordance with results found in (Faltinsen and Timokha, 2009),(Zhao et al., 2013) and (Hu et al., 2017). The effect of elasticity in the model seems

to be limited in heave, as the RAOs for model K21 and K11 are more or less equal (see Figure 4.3d). The RAOs calculated at low periods seems to be a tiny bit higher for the elastic model K21 than for the rigid model K11. However, the RAOs are so small in this area that it does not affect the response of the structure particularly much.

Kristiansen et al. (2018b) found that reflections from radiated and diffracted waves from the tank-wall affected the results significantly. This effect is clearly visible in the RAO calculations done in this thesis as well. There are several spikes that appear around the natural frequency, and also a clear canceling effect around T=1.5s that are most likely appearing due to tank-wall effects. The tank-wall effect is discussed further below in Section 4.2.5.

Wave steepness seems to have little effect on the response in heave for low periods. In the upper area of the periods tested, the response deviates slightly, indicating that there might be a small dependence on the wave steepness in this area.

The calculated RAOs for the Heave motions corresponds well with the results presented in (Kristiansen et al., 2018a).

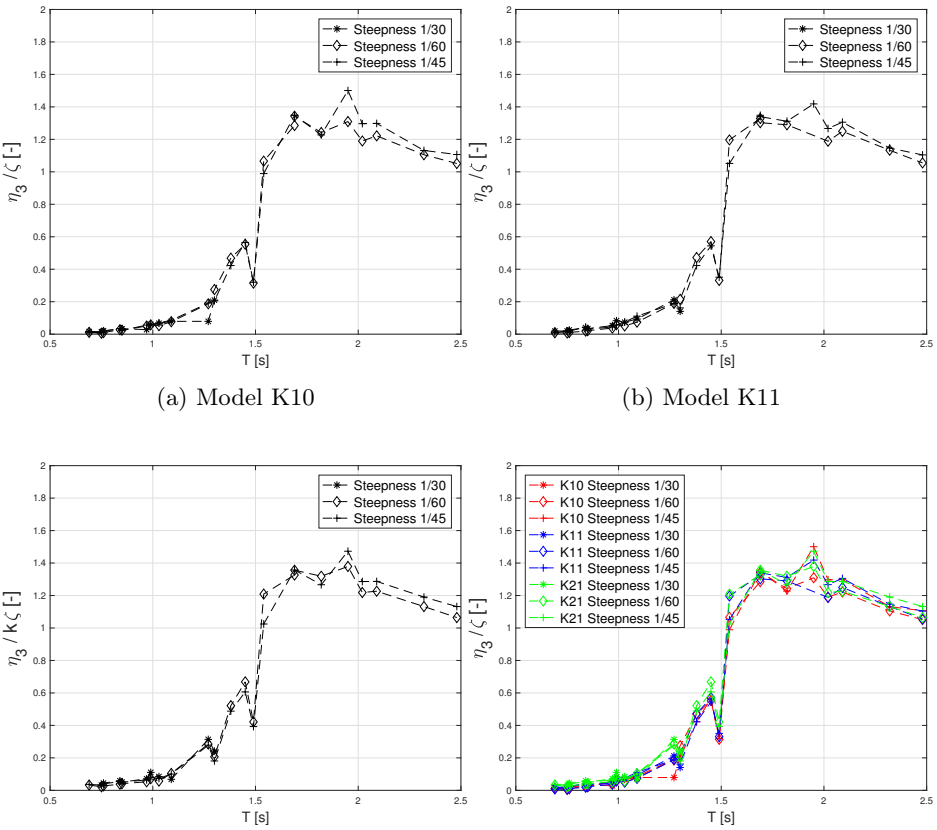

(a) Model K10

(b) Model K11

(c) Model K21

(d) Comparison of the three models

Figure 4.3: RAO in Heave calculated with experimental values for the three models K10, K11 and K21

4.2.3 RAO in Pitch

Figure 4.4 shows how the RAOs changes form with the included water. K10 has a clear peak at the natural period at T=1.7s, while the two other models have a more rounded curve. The internal liquid has a destabilizing effect on the structure, which leads to an increase in the natural period. K11 and K21 have the same form up until about T=1.9s where K21 keeps the same amplitude, while K11 drops off a slightly. The reason for why the curves for K11 drops off while the ones for K21 stays at the same level is unclear, but could be due to the elasticity

in model K21.

The RAOs for K21 and K11 peaks at about T=2s, with an amplitude of 0.5. Furthermore, one can see that the peak value for the dry model is about 2.1 (see Figure 4.4c and Figure 4.4b respectively).

There is no clear trend indicating an effect of the wave steepness in pitch for model K10 and K21. For model K11, the RAOs for low frequencies are significantly affected by wave steepness as seen in Figure 4.4b.

Another interesting factor is that the RAOs at the second sloshing mode (T=1.07s) are almost twice as big for the wet models(K21 and K11) as for the dry model (K10).

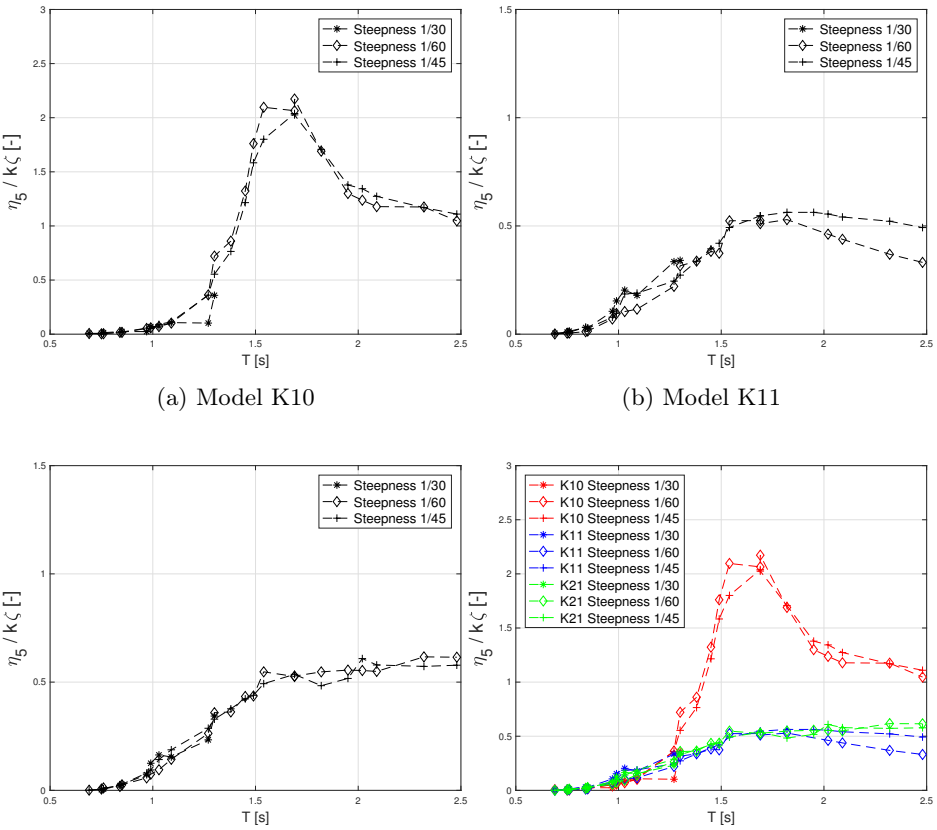

(a) Model K10

(b) Model K11

(c) Model K21

(d) Comparison of the three models

Figure 4.4: RAO in Pitch calculated with experimental values for the three models K10, K11 and K21

4.2.4 Sloshing

The RAOs for sloshing are presented for model K11 and K21 in Figure 4.5 and Figure 4.6 respectively. The RAOs are calculated for the five internal positions illustrated in Figure 3.3, and for the same three wave steepnesses used for the heave, surge and pitch calculations. The position numbers used in this section are the ones presented in Figure 3.3.

There seems to be a clear connection between the wave steepness and the ampli-

tude measured at the natural frequency. This connection might be the reason for why the responses for the same periods are dependent on wave steepness. The dependence of wave steepness is clearly visible for wave periods in the area of 0.75s, where three of the natural periods for the contained liquid are found (T=0.756s, T=0.757s, and T=0.860s). Due to the low resolution of measurements in this area, it is difficult to identify all three natural modes. However, there are no doubts regarding the presence of at least one natural period in that particular area.

The modal shape for the natural period of 0.907s, calculated by linear sloshing theory and presented in Figure 4.1, has a peak value in the center of the structure and a very low value at the edge. Looking at Figure 4.5 the measurements at the edge gives a RAO close to zero, which confirms the modal shape presented Figure 4.1a.

The two highest natural periods give clear peaks in the free surface elevation. The highest natural period has clearly higher values at the front and back of the structure (Pos1 and Pos5). This is an expected result looking at the modal shapes found in Figure 4.1.

Comparing the RAO of the elastic model with the rigid model, it can be observed a significant amplification of the amplitudes around the natural period of 1.042s. This amplification corresponds well with the elastic deformation amplitudes calculated for the model. Furthermore, the response of higher periods are lower for the elastic model than for the rigid model on average. Looking at the curve for the elastic deformations for K21, presented in (Kristiansen et al., 2018a), it easy to see how this corresponds to the difference between K11 and K21.

Some general remarks that are worth noting are that the RAOs for sloshing are generally higher for Position 1 and 5 than for the rest of the structure. Furthermore, there are no natural periods for high incident wave periods. This corresponds well with the findings in Section 4.1, where the highest natural period is 1.502s. The sloshing RAOs calculated corresponds well with the RAOs presented in (Kristiansen et al., 2018a).

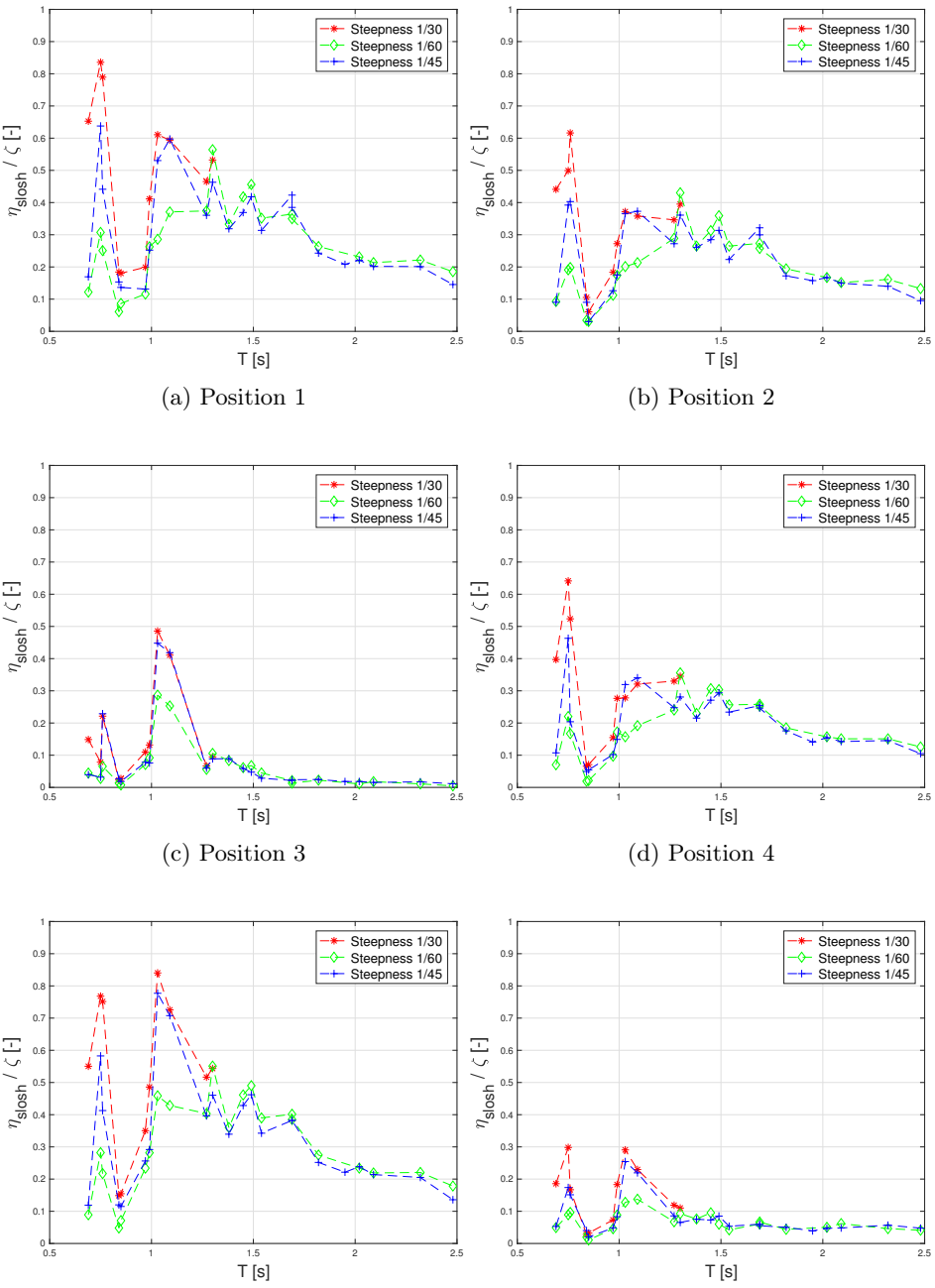

(a) Position 1

(b) Position 2

(c) Position 3

(d) Position 4

(e) Position 5

(f) Position 6

Figure 4.5: Sloshing RAO for the six different WP for model K11

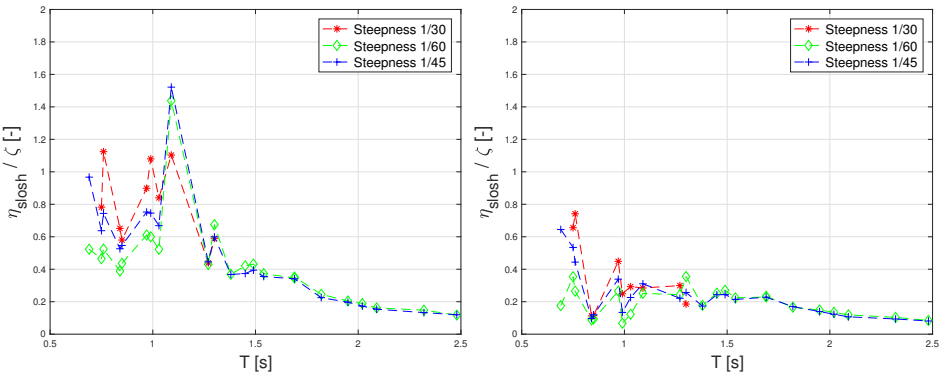

(a) $T_{0,1} = 0.907$s (b) $T_{1,1} = 1.502$s

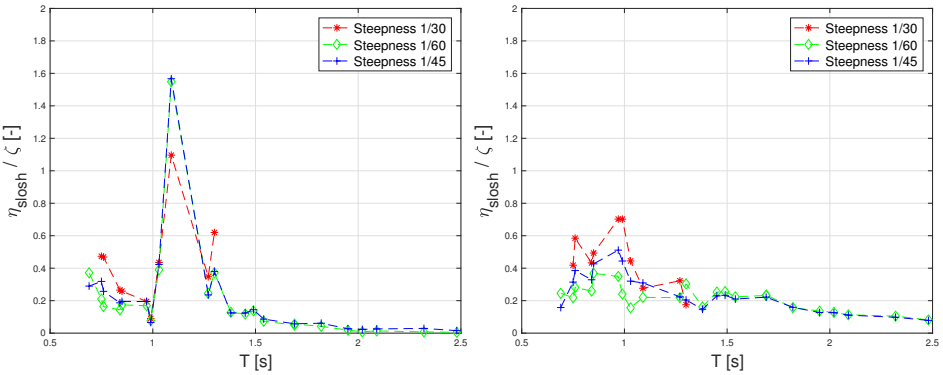

(c) $T_{2,1} = 1.042$s (d) $T_{1,2} = 0.756$s

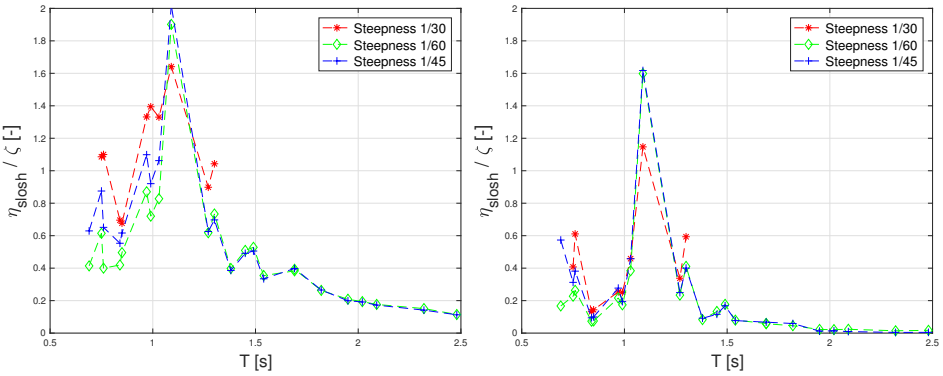

(e) $T_{3,1} = 0.860$s (f) $T_{4,1} = 0.757$s

Figure 4.6: Sloshing RAO for the six different WP for model K21

4.2.5 Error Sources

There will always be errors present when an experiment is conducted, but the effect from the different error sources on the final results vary significantly. The most prominent error source in the SJØFLO experiment is the tank-wall effect, which has been thoroughly described in (Kristiansen et al., 2018a) and (Kristiansen et al., 2018b). The radiated waves of the tank-walls may interfere with the structure response, which might lead to a cancellation- or an amplification effect on the response of the structure. One way to reduce the tank-wall effect is to reduce the scaling-factor. However, having a smaller model implies that measurement errors will have a greater impact.

The Oculus measuring device has a small error as well, something clearly visible for high frequency, low amplitude waves. Filtering the raw-data may also introduce a small error. However, these error contributions can more or less be neglected as the RAOs for the smallest waves are so small. Finally, Table 3.2 confirms that the different WP have a slightly different value as well.

4.3 Potential theory - WADAM

This section contains a comparison between the RAOs calculated from the experimental values and the RAOs calculated with the potential theory software WADAM. The RAOs are calculated in Heave, Pitch and Surge for both a dry model (K10) and a wet model (K11). Input values for the numerical calculations can be found in Section 2.4, and the experimental results for all three wave steepnesses are used.

Surge

The RAO calculated with potential theory gives a good representation in surge for periods up to 1.5s for model K10 as seen in Figure 4.7. However, the cancellation effect appears earlier in the numerical software than in the model experiment. For periods above 1.7 seconds, the potential theory curve follows the same curve as the experimental values with a small continuous deviation. The deviation observed here is slightly larger than the one calculated with WAMIT in (Kristiansen et al., 2018a). The reason for why the deviation is larger in the WADAM calculations might be because the solvers of the internal liquid problem are slightly different,

it is more likely, however, due to a slight difference in the model.

In Figure 4.8 it can be observed that potential theory gives a great representation up until periods of 2 seconds. At just above two seconds, potential theory gives a full cancellation in response before a resonance effect appears. This corresponds well with the results presented in (Kristiansen et al., 2018a); however, the cancellation and following the resonance effect appears at periods that are about 0.3 seconds lower.

The reason for why potential theory gives such a high peak at T=2.1s for model K11 is due to the lack of viscous damping described in Section 2.3.2.

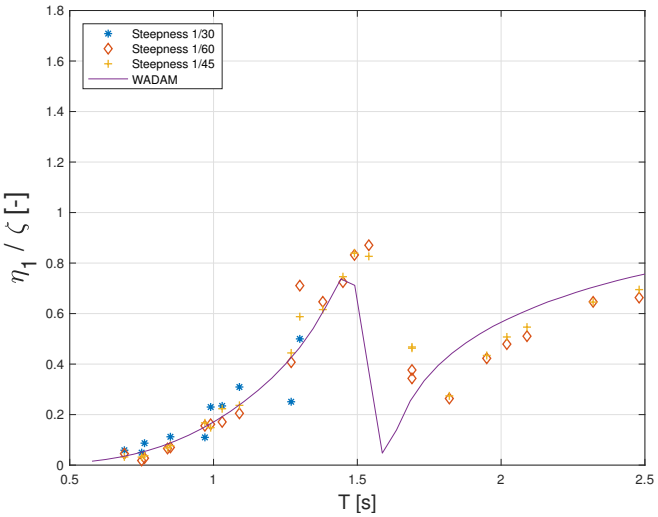

Figure 4.7: Comparison of potential theory (WADAM) and model experiment for model K10 in Surge

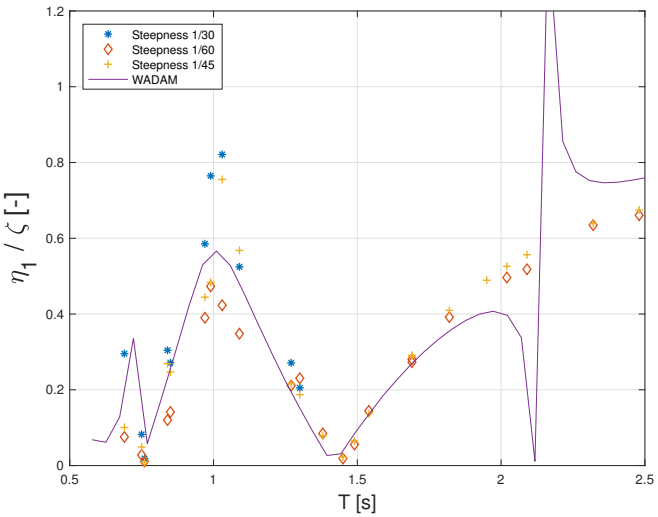

Figure 4.8: Comparison of potential theory (WADAM) and model experiment for model K11 in Surge

Heave

As seen in Figure 4.9 and Figure 4.10, potential theory give a very good representation of the response in heave. The small extension in the peak value is due to the absence of viscous damping.

The effect of sloshing on the heave motion is close to zero. As shown in Section 4.2.2, the RAOs for model K10 and K11 are equal for all practical applications. This is very much in accordance with the results presented in (Kristiansen et al., 2018a), and also with the definition of potential theory. The vertical sides of the FCCS are anticipated not to affect sloshing if potential theory is assumed valid, which is confirmed by looking at Figure 4.9 and Figure 4.10.

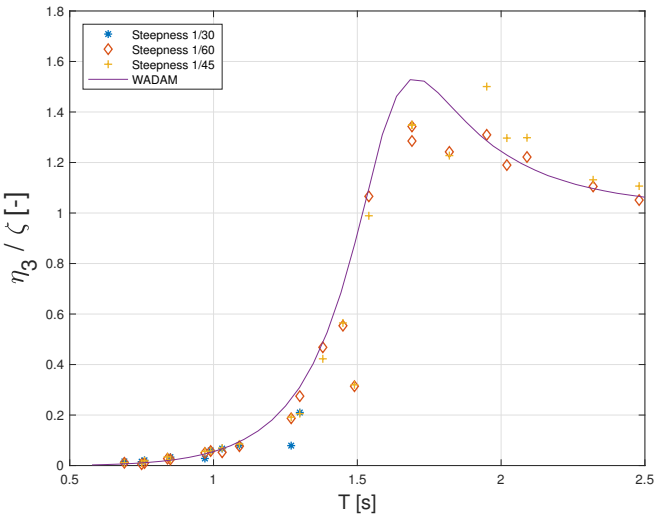

Figure 4.9: Comparison of potential theory (WADAM) and model experiment for model K10 in Heave

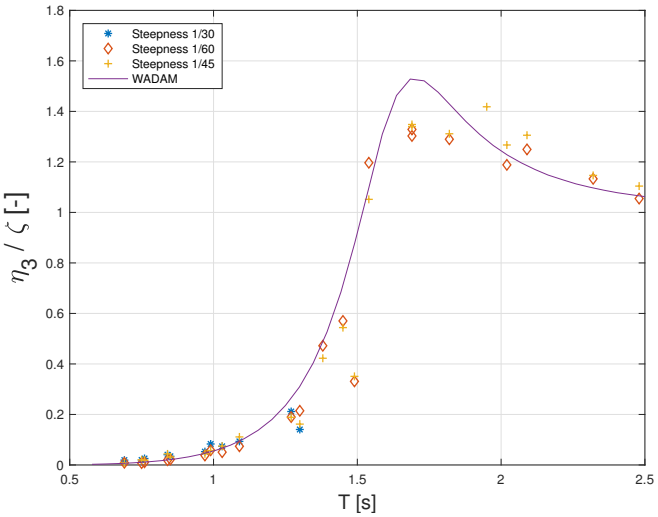

Figure 4.10: Comparison of potential theory (WADAM) and model experiment for model K11 in Heave

Pitch

RAOs in pitch are not represented particularly good with potential theory. By looking at Figure 4.11 and Figure 4.12, a significant deviation between the experimental values and the potential theory values can be seen.

Although the RAOs presented in this thesis resembles the ones presented (Kristiansen et al., 2018b), they are still quite far off the experimental values. For model K11 a peak is located at T=2.25s, and cancellation of response is located at T=1.95s. Both the peak and the cancellation of response are not present in the experimental values as seen in Figure 4.12. Furthermore, the natural period for the numerical calculations looks to appear at about half of the period of the experimental values, which is hard to explain why.

For model K10, the results are slightly better. The peak at the natural period is much higher for the numerical calculations as no viscous damping is present. However, the reason for why the response is higher for the numerical calculations at low frequencies and lower at high frequencies is hard to explain.

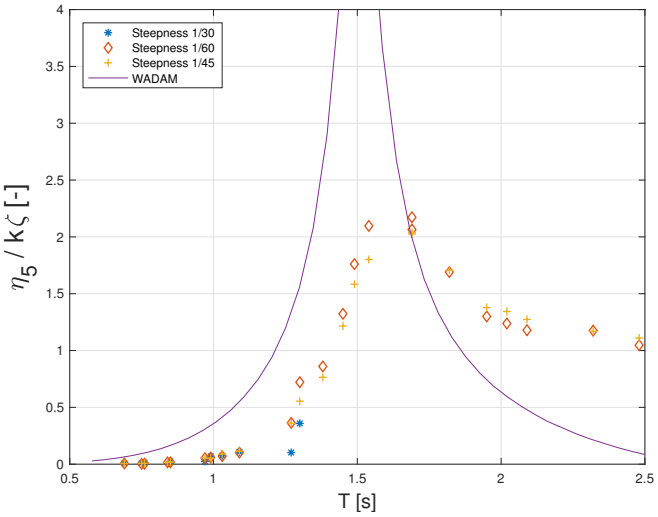

Figure 4.11: Comparison of potential theory (WADAM) and model experiment for model K10 in Pitch

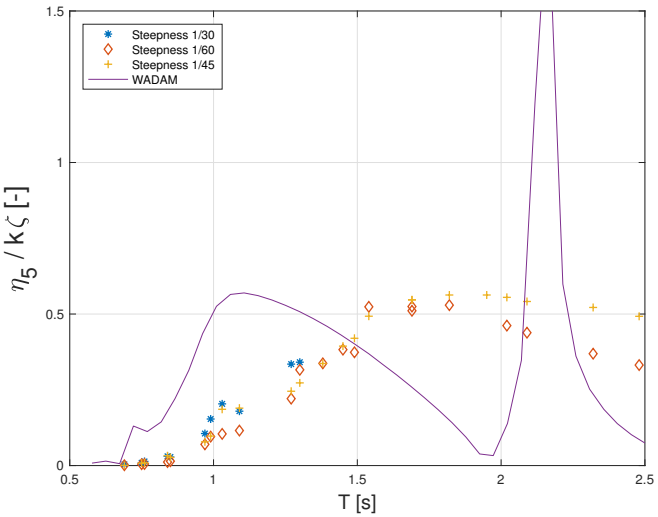

Figure 4.12: Comparison of potential theory (WADAM) and model experiment for model K11 in Pitch

4.4 The dome

The original plan was to analyze a spherical shaped FCCS (the dome) with the same floating collar and mooring system like the one used in the SJØFLO experiment. However, when this concept was modeled in GeniE and analyzed in WADAM, the software gave the output "negative GM-value" when the effect of the free surface was applied. Negative GM-value indicates that the system is unstable. As part of the search for the source of this error, a control run was conducted with a spherical tank without floating collar. This control run gave positive GM, which is very strange as a completely spherical shape should give a GM value of zero. The reason for why this value was positive might be because of imperfections in the geometry due to the mesh not being perfectly spaced out.

To compensate for the negative GM, a much bigger floating collar was added. When the floating collar reached 0.25m out from the cage-wall, it gave a positive GM-value for both 50% filling and 75% filling. However, for the 90% filling level, it was still negative. As the extended floating collar is almost 10 times as wide as the original one, it was decided not to make it any bigger and rather look at the results obtained with this collar for 50% and 75% filling level.

In the following figures, the numerical calculations of a dry and a wet dome are plotted for 50% and 70% filling levels in surge, heave, and pitch.

Surge

For the dome model with 50% filling ratio, the RAOs in surge resembles the ones obtained for the circular cylinder. However, as the floating collar is much bigger, the potential damping will also be bigger. Therefore the peak that appears at T=2.2s for the circular cylinder is damped out in Figure 4.13. The reason for why the natural period is slightly moved to the left for both the dry and the wet model with 50% filling level compared to the circular cylinder might be due to a small change in the structural mass.

Comparing the natural periods of dry and wet models with 50% and 75% filling level, both increase due to the increased mass. For the wet model it increases from 0.95s to 1.5s, and for the dry model, it increases from 1.25s to 1.75s. The maximum amplitude of the wet model is more or less constant, while for the dry model the amplitude is almost ten times as big. Now, in a real-world scenario, the viscous damping would most likely reduce this peak significantly.

It is interesting to see that two smaller peaks appear at about 0.75s and 1.0s for the wet model with 75% filling level. These two peaks appear most likely due to sloshing.

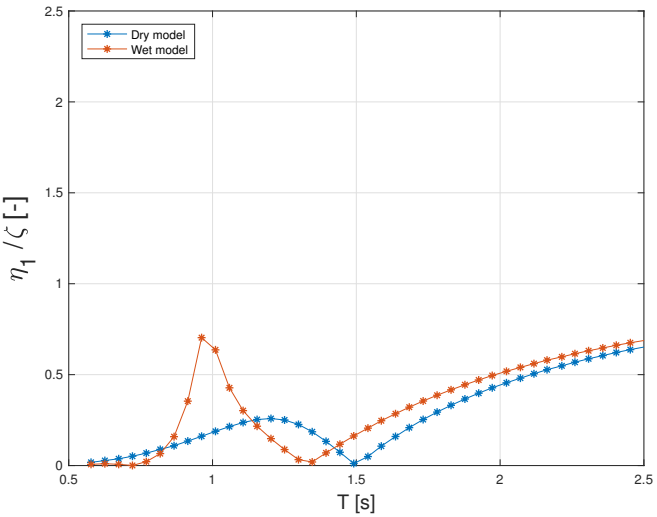

Figure 4.13: Comparison of wet and dry dome with 50 % filling, Surge

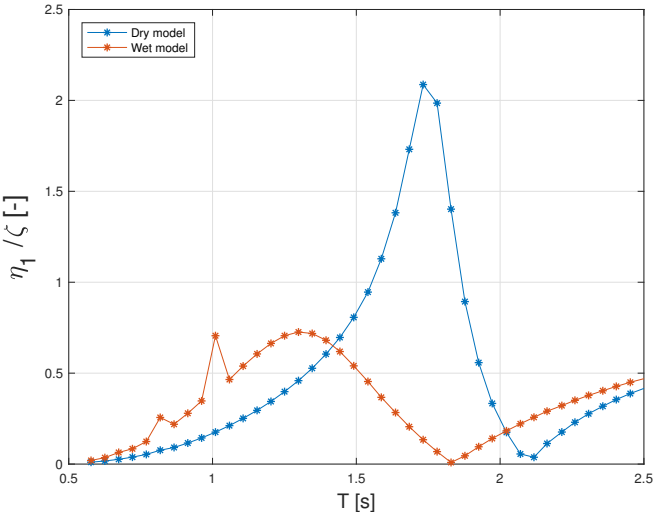

Figure 4.14: Comparison of wet and dry dome with 75 % filling, Surge

Heave

Looking at both Figure 4.15 and Figure 4.16 it is clear to see that the effect of sloshing is absent in both the model with 50% and 75% filling levels. This result is very much in accordance with the definitions of potential theory, and can also be seen for the circular cylinder model presented above.

For the model with 50% filling level, the potential damping is large enough to damp out the motion at the natural period. The same cannot be said for the model with 75% filling level, as it gets a peak at about 1.7s.

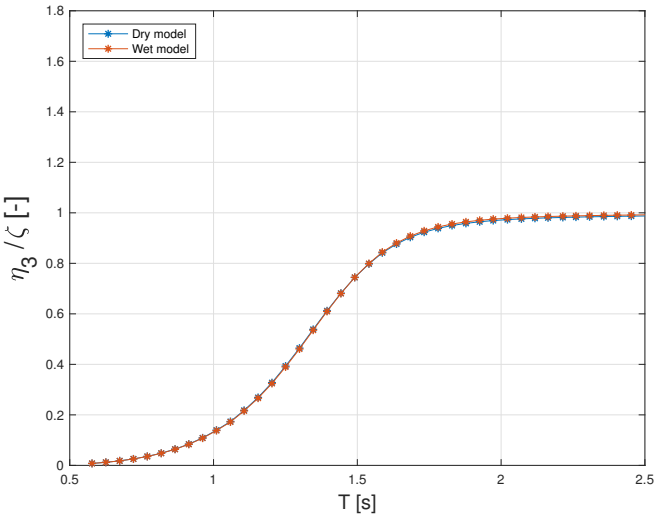

Figure 4.15: Comparison of wet and dry dome with 50 % filling, Heave

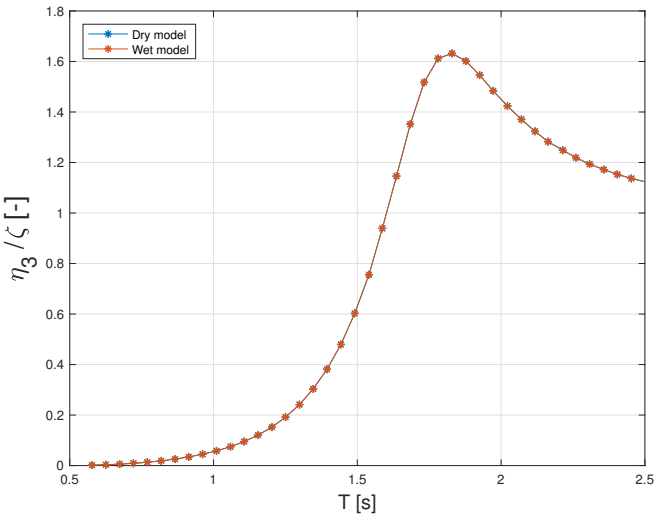

Figure 4.16: Comparison of wet and dry dome with 75 % filling, Heave

Pitch

Pitch follows a similar pattern as surge, with two small peaks for the model 75% filling level before the natural period, at about T=0.8s and T=1.0s. Furthermore, the amplitude for the dry model is increased a lot, together with the natural period. The wet model has a much larger increase in pitch amplitude than seen in surge motion. The cancellation of response found at T=1.0s for the model with 50% filling level is replaced by a natural period for the model with 75% filling level. This is very interesting, as the increased filling level seems to affect the modal shape of the sloshing.

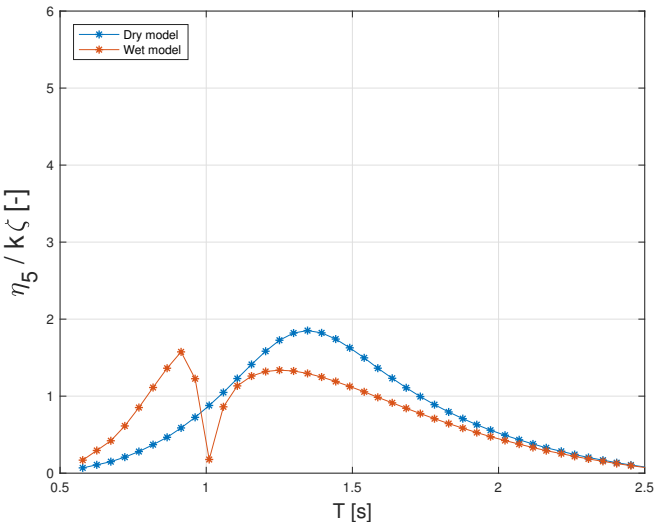

Figure 4.17: Comparison of wet and dry dome with 50 % filling, Pitch

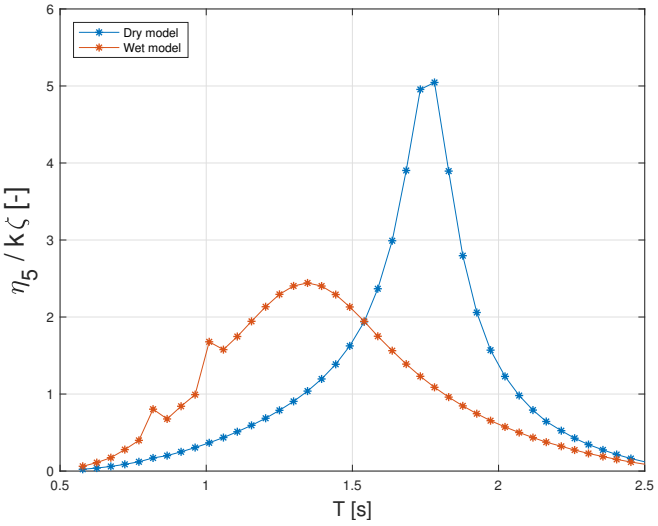

Figure 4.18: Comparison of wet and dry dome with 75 % filling, Pitch

Chapter 5

Conclusion

In the literature study, several methods for sloshing suppression were presented, of which some had the potential to work in a FCCS. A FCCS with changing filling level was selected for further study with numerical calculations, and the theory for damping due to baffle rings was presented. Due to the time limit of this thesis, and the authors lack of experience within CFD calculations, the effect of the baffle ring on such a big volume structure was not included. Analyzing the effect of filling level within the spherical model proved to be a lot harder than expected, as WADAM gave an unstable system until the floating collar was increased by a tenfold. The fact that the floating collar had to be increased that much made it hard to compare the structure with the experimental results obtained for the circular model.

The results found in this thesis concur very well with the results presented in (Kristiansen et al., 2018a). The analysis of the experimental data seems to be more or less equal to the results presented in the end report, however, the numerical calculations deviate more. Some of the reasons for these deviations are related to the fact that the computer models have been made in two different programs. The model used in this thesis is based on presented values in (Kristiansen et al., 2018a), without seeing the complete model. Some deviations might be explained by the different solvers for internal liquid as well, but this not as certain.

There is a significant effect of sloshing on the rigid body motions calculated from both the numerical software and the experimental values. Surge motion triggers several of the natural periods of the internal liquid, especially in the low period

area. In pitch, the internal liquid has a destabilizing effect on the structure, hence the increased natural period and lowered peak value. Heave is not influenced by sloshing, which is expected as the bottom is far from the free surface and the vertical walls will not induce sloshing motion. The same pattern can be seen in both the potential theory and the experimental results. However, the absence of viscous damping in potential theory gives a very high amplitude that would normally be damped out.

The issues with negative GM-value for the dome model was not expected, as no issues were experienced for the circular cylinder. No proper reason was found for why this error occurred, and hand-calculations gave positive GM. Thus, care should be taken if WADAM is to be used for wave structure analyses where the tank volume to structure volume ratio is as high as in this example.

Chapter 6

Recommendations for further work

With the FCCSs being such novel structures, several aspects must be studied further to ensure safe constructions that can maintain fish well-fare in harsh weather conditions. Further work should, of course, be conducted on the effect of sloshing, and how to keep the sloshing within reasonable boundaries. Furthermore, the operational changes that follow, when the walls of the fish farm are being closed, should also be studied. As mentioned earlier, keeping the water quality at a certain level is probably the most critical part of the whole FCCS. Thus, control systems for the water parameters must be developed and tested.

A more specific list of recommendations for further work can be found below:

1. CFD analysis of the baffle ring to better document the effect in terms of sloshing suppression.
2. Model scaled experiments of the dome model.
3. Fatigue analysis of the elastic cage used in this experiment.
4. Document the effects of waves on fish well-fare. Should there be an upper limit with regards to internal wave height, for instance?

Bibliography

Abramson, H. (1969). Slosh suppression. Technical report, Natinal Aeronautics and space administration.

Abramson, H. N. (1966). The dynamic behavior of liquids in moving containers with applications to space vehicle technology. Technical report, NASA; United States.

Almaas, K. A., Abildgaard, C., Elvevoll, E., Krog, J., Nordhammer, L. I., Olsen, Y., Soerensen, A. J., and Overskaug, K. (2012). *Verdiskaping basert på produktive hav i 2050*. NTVA and DKNVS.

Bergheim, A., Seymour, E. A., Sanni, S., Tyvold, T., and Fivelstad, S. (1992). Measurements of oxygen consumption and ammonia excretion of atlantic salmon (salmo salar l.) in commercial-scale, single-pass freshwater and seawater landbased culture systems. *Aquacultural Engineering*.

Boulet, D., Struthers, A., and Gilbert, E. (2010). Feasibility study of closed-containment options for the british columbia aquaculture industry. Technical report, Fisheries and Oceans Canada.

Chadwick, E. M. P., Parsons, G. J., and Sayavong, B. (2010). *Evaluation of Closed-containment Technologies for Saltwater Salmon Aquaculture*. NRC Research Press Ottawa.

DNVGL (2015). *SESAM user manual - WADAM*, 13 edition.

Faltinsen, O. M. (1998). *Sea Loads On Ships And Offshore Structures*. Cambridge University press.

Faltinsen, O. M. and Timokha, A. N. (2009). *Sloshing*. Cambridge University press.

Food and Agriculture Organization of the United Nations (2016). *The state of world fisheries and aquaculture 2016*. FAO.

Garza, L. R. and Abramson, H. N. (1963). Measurements of liquid damping provided by ring baffles in cylindrical tanks. Technical report, NASA; United States.

Graven, A. R. (2016). New trials: improved fish health and more efficient production. `http://ctrlaqua.no/news/2016/06/03/new-trials-improved-fish-health-and-more-efficient-production/`. Accessed: 2018-19-05.

Hosfeld, C. D., Hammer, J., Handeland, S. O., Fivelstad, S., and Stefansson, S. O. (2009). Effects of fish density on growth and smoltification in intensive production of atlantic salmon (salmo salar l.). *Elsevier Aquaculte*.

Hu, Z.-Q., Wang, S.-Y., Chen, G., Chai, S.-H., and Jin, Y.-T. (2017). The effects of lng-tank sloshing on the global motions of flng system. *International Journal of Naval Architecture and Ocean Engineering*, 9(1):114–125.

Ibrahim, R. A. (2005). *Liquid Sloshing Dynamics*. Cambridge University press.

JR, S. R. H. and Abramson, H. N. (1959). Hydroelasticity: A new naval science. *Journal of the American Society for Naval Engineers*, 71:205–209.

Keulegan, G. H. and Carpenter, L. H. (1958). Forces on cylinders and plates in an oscillating fluid. *Journal of Research of the National Bureau of Standards*, 60(5).

Kristiansen, D., Endresen, P. C., Lader, P., Su, B., Volent, Z., and Aksnes, V. (2018a). Sjøflo - sjøegenskaper og forankring til flytende lukkede oppdrettsanlegg. Technical report, Sintef Ocean.

Kristiansen, D., Lader, P., Endresen, P. C., and Aksnes, V. (2018b). Numerical end experimental study on the seakeeping behavior of floating closed rigid fish cages. *Submitted to OMAE2018-77254*.

Kristiansen, D., Lader, P., Jensen, Øysten., and Fredriksson, D. (2015). Experimental study of an aquaculture net cage in waves and current. *China Ocean Eng.*, 29(3).

Lader, P., Bjelland, H. V., Kristiansen, D., Alver, M., and Myrhaug, D. (2017). Classification of aquaculture locations in norway with respect to wind wave exposure. *OMAE2017-61659*.

Morison, J., Obrien, M., Johnson, J., and Schaaf, S. (1950). The force exerted by surface waves on piles. *Petroleum transactions, AIME*, 189.

Newland, D. (1981). *An introduction to Random Vibrations and Spectral Analysis*. Longman inc.

Newman, J. (1962). The exciting foreces on fixed bodies in waves. *Journal of Ship Research, Society of Naval Architects and Marine Engineers*, 6(3).

Newman, J. (1977). *Marine Hydrodynamics*. The MIT press.

Ochi, M. K. (1990). *Applied Probability and Stochastic Processes*. John Wiley and sons.

Rosten, T. W., Ulgenes, Y., Henriksen, K., Terjesen, B. F., Biering, E., and Winther, U. (2011). Oppdrett av laks og ørret i lukkede anlegg - forprosjekt. Technical report, Sintef Fiskeri og Havbruk.

Said, M. E. M., Arif, U. G. M., Kamaruddin, M. H., Kee-Quen, L., and Hooi-Siang, K. (2017). Suppression of sloshing in liquified natural gas during ocean-going transportation by using speherical floaters and blanket. *Journal of Transport System Engineering*, 4(1).

Standard Norway (2009). Norwegian standard for floating aquaculture facilities. Technical report, Standard Norway.

Steen, S. (2014). Tmr7 experimental methods in marine hydrodynamics, lecture notes. `http://www.ivt.ntnu.no/imt/courses/tmr7/lecture/Scaling_Laws.pdf`. Accessed: 2018-19-05.

Steinset, T. A. (2017). Fiskeoppdrett i norge og verden. `https://www.ssb.no/jord-skog-jakt-og-fiskeri/artikler-og-publikasjoner/fra-attatnaering-til-milliardindustri`. Accessed: 2018-26-04.

Sundar, D. V. (2016). *Ocean Wave Mechanics*. Wiley.

The editorial team, Hegnar.no (2016). Costs related to salmon lice has exploded. `http://www.hegnar.no/Nyheter/Naeringsliv/2016/03/Dette-koster-norske-bedrifter-fem-milliarder-i-aaret`. Accessed: 2018-09-04.

Thorarensen, H. and Farrell, A. P. (2011). The biological requirements for post-smolt atlantic salmon in closed-containment systems. *Aquaculture*, 312(1-14).

Thorbjørnsen, K. E. and Litland, K. E. (2017). Development licenses register. `https://www.fiskeridir.no/Akvakultur/Tildeling-og-tillatelser/Saertillatelser/Utviklingstillatelser`. Accessed: 2018-09-04.

Yang, H. Q. and West, J. (2016). Investigation of damping physics and cfd tool validation for simulation of baffled tanks at variable slosh amplitude. Technical report, NASA; United States.

Zhao, W., Yang, J., and Hu, Z. (2013). Effects of sloshing on the global motion responses of flng. *Ships and Offshore Structures*, 8(2):111–122.

List of Appendices

Appendix A Model scale test conditions II

Appendix B Steady State periods III

Appendix C Computer models V

A Model scale test conditions

In Table 6.1 the test conditions used in the SJØFLO experiment can be found. All values in this table are given in model scale.

Table 6.1: Model scale test conditions

λ/D	**Wave period**	**Wave height H[m]**		
[-]	T [s]	$\epsilon = 1/30$	$\epsilon = 1/45$	$\epsilon = 1/60$
0,49	0,69	0,025	0,016	0,012
0,58	0,75	0,029	0,019	0,014
0,59	0,76	0,030	0,020	0,015
0,74	0,84	0,037	0,025	0,019
0,76	0,85	0,038	0,025	0,019
0,99	0,97	0,049	0,033	0,025
1,03	0,99	0,051	0,034	0,026
1,11	1,03	0,056	0,037	0,028
1,23	1,09	0,062	0,041	0,031
1,68	1,27	0,084	0,056	0,042
1,76	1,30	0,088	0,059	0,044
1,98	1,38	0,099	0,066	0,049
2,19	1,45	0,110	0,073	0,055
2,31	1,49	0,116	0,077	0,058
2,47	1,54	0,123	0,082	0,062
2,96	1,69	0,148	0,099	0,074
2,97	1,69	0,149	0,099	0,074
3,46	1,82	0,173	0,115	0,086
3,95	1,95	0,198	0,132	0,099
4,24	2,02	0,212	0,141	0,106
4,53	2,09	0,227	0,151	0,113
5,58	2,32	0,279	0,186	0,140
6,43	2,48	0,321	0,214	0,161

B Steady State periods

The following table (6.2) provides the beginning and end of the steady state period for each of the 23 wave conditions used in the test. The beginning and end are presented as the length of time series so that 1 is the very end of the time series, and 0 is the beginning. The wave periods are presented in model scale.

Table 6.2: Table indicating the steady state period for each of the 23 wave scenarios

Wave period (T [S])	Start of steady state	End of steady state
0,69	0,52	1
0,75	0,49	1
0,76	0,48	1
0,84	0,44	1
0,85	0,45	1
0,97	0,39	0,94
0,99	0,39	0,93
1,03	0,38	0,89
1,09	0,36	0,85
1,27	0,32	0,74
1,30	0,32	0,72
1,38	0,31	0,68
1,45	0,30	0,65
1,49	0,29	0,63
1,54	0,29	0,61
1,69	0,27	0,57
1,69	0,27	0,56
1,82	0,26	0,53
1,95	0,25	0,50
2,02	0,25	0,48
2,09	0,25	0,47
2,32	0,24	0,42
2,48	0,23	0,34

A shortened steady state period was also tested. The shortened steady state was used to confirm that the steady state period originally considered was in fact at steady state. The shortened steady state period can be found in table 6.3.

Table 6.3: Table indicating the shortened steady state period for each of the 23 wave scenarios

Wave period (T [S])	Start of steady state	End of steady state
0,69	0,6398	0,8799
0,75	0,6148	0,8716
0,76	0,6108	0,8703
0,84	0,5797	0,8599
0,85	0,5763	0,8588
0,97	0,5304	0,8058
0,99	0,5215	0,7911
1,03	0,5046	0,763
1,09	0,4832	0,7272
1,27	0,4269	0,6324
1,3	0,4187	0,6185
1,38	0,4009	0,588
1,45	0,3854	0,5616
1,49	0,3778	0,5484
1,54	0,3688	0,5329
1,69	0,3456	0,4923
1,69	0,3453	0,4917
1,82	0,328	0,4608
1,95	0,314	0,4356
2,02	0,3071	0,4231
2,09	0,3008	0,4114
2,32	0,2832	0,378
2,48	0,2727	0,3575

C Computer models

Figure 6.1 illustrates the meshed circular cylinder model as presented in the modelling program GeniE.

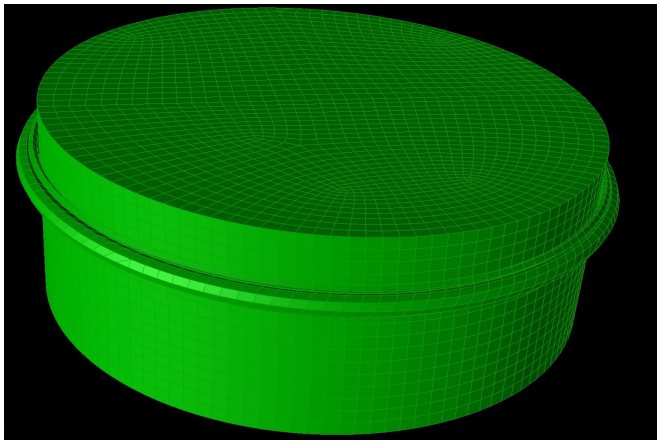

Figure 6.1: Model in GeniE

Figure 6.2 illustrates how the final circular cylinder model looks during an analysis in WADAM.

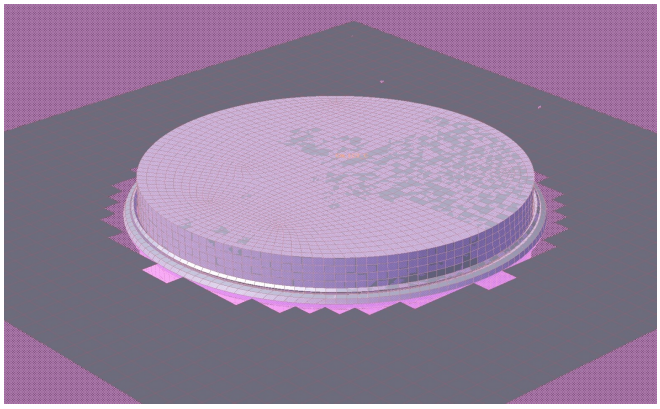

Figure 6.2: Circular cylinder presented in WADAM

Figure 6.3 illustrates the meshed dome model as it appears in the modelling program GeniE.

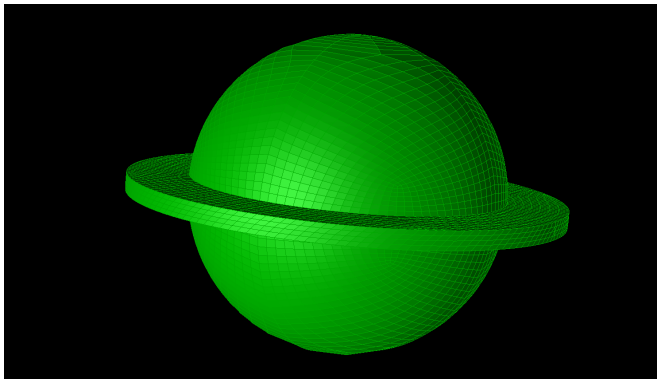

Figure 6.3: Model in GeniE

Figure 6.4 illustrates how the final dome model looks during an analysis in WADAM.

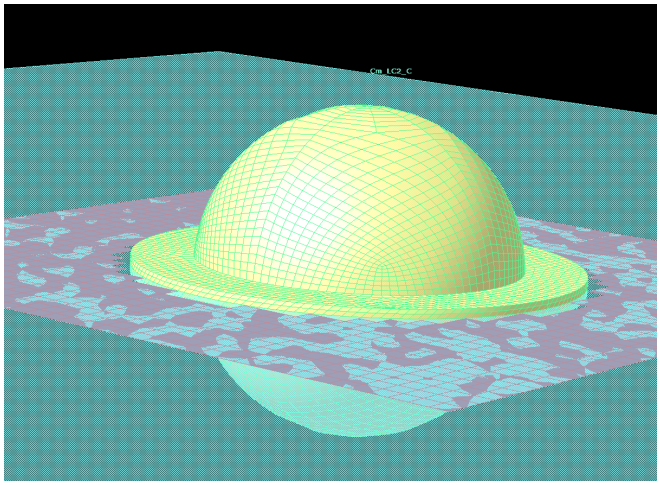

Figure 6.4: Circular cylinder presented in WADAM